



ORIGINAL RESEARCH

Protective Functions of Liver X Receptor α in Established Vulnerable Plaques: Involvement of Regulating Endoplasmic Reticulum–Mediated Macrophage Apoptosis and Efferocytosis

Xinyu Che, MS*; Qingqing Xiao, MS*; Wei Song, MD, PhD*; Hengyuan Zhang, BS; Beibei Sun , MD, PhD; Na Geng, BS; Zhenyu Tao, MS; Qin Shao , MD, PhD; Jun Pu, MD, PhD

BACKGROUND: Liver X receptor (LXR) belongs to the metabolic nuclear receptor superfamily, which plays a critical regulatory role in vascular physiology/pathology. However, effects of systemic LXR activation on established vulnerable plaques and the potential isotype-specific role involved remain unclear.

METHODS AND RESULTS: The 8-week-old male apolipoprotein E^{-/-} mice went through carotid branch ligation and renal artery constriction, combined with a high-fat diet. Plaques in the left carotid artery acquired vulnerable features 4 weeks later, confirmed by magnetic resonance imaging scans and histological analysis. From that time on, mice were injected intraperitoneally daily with PBS or GW3965 (10 mg/kg per day) for an additional 4 weeks. Treatment with LXR agonists reduced the lesion volume by 52.61%, compared with the vehicle group. More important, a profile of less intraplaque hemorrhage detection and necrotic core formation was found. These actions collectively attenuated the incidence of plaque rupture. Mechanistically, reduced lesional apoptosis, enhanced efferocytosis, and alleviated endoplasmic reticulum stress are involved in the process. Furthermore, genetic ablation of LXR α , but not LXR β , blunted the protective effects of LXR on the endoplasmic reticulum stress–elicited C/EBP-homologous protein pathway in peritoneal macrophages. In concert with the LXR α -predominant role in vitro, activated LXR failed to stabilize vulnerable plaques and correct the acquired cellular anomalies in LXR α ^{-/-} apolipoprotein E^{-/-} mice.

CONCLUSIONS: Our results revealed that LXR α mediates the capacity of LXR activation to stabilize vulnerable plaques and prevent plaque rupture via amelioration of macrophage endoplasmic reticulum stress, lesional apoptosis, and defective efferocytosis. These findings might expand the application scenarios of LXR therapeutics for atherosclerosis.

Key Words: atherosclerosis ■ endoplasmic reticulum stress ■ liver X receptor α ■ macrophage ■ vulnerable plaque

Atherothrombosis and the subsequent occlusion of arteries, which give rise to acute coronary syndrome or stroke, have been the leading causes of death in the world. These adverse clinical events are highly correlated with plaque vulnerability in a

thrombosis-promoting milieu.¹ Specifically, vulnerable plaques, which have several features, including arterial outward remodeling, intraplaque hemorrhage, necrotic core formation, and inflammatory cell accumulation,^{2,3} are prone to rupture and precipitate thrombotic events.

Correspondence to: Qin Shao, MD, PhD, Renji Hospital, School of Medicine, Shanghai Jiao Tong University, 160 Pu Jian Rd, Shanghai, China 200127. E-mail: shaoqindr@126.com

*X. Che, Q. Xiao, and W. Song contributed equally and are joint first authors.

Supplementary Material for this article is available at <https://www.ahajournals.org/doi/suppl/10.1161/JAHA.120.018455>

For Sources of Funding and Disclosures, see page 17.

© 2021 The Authors. Published on behalf of the American Heart Association, Inc., by Wiley. This is an open access article under the terms of the Creative Commons Attribution-NonCommercial-NoDerivs License, which permits use and distribution in any medium, provided the original work is properly cited, the use is non-commercial and no modifications or adaptations are made.

JAHA is available at: www.ahajournals.org/journal/jaha

CLINICAL PERSPECTIVE

What Is New?

- Activating liver X receptor (LXR) reduces vulnerable features and prevents plaque rupture in preexisting unstable lesions.
- LXR activation alleviates apoptosis and defective efferocytosis as well as endoplasmic reticulum stress in carotid vulnerable plaques.
- LXR α inhibits the endoplasmic reticulum stress-mediated CHOP pathway in macrophages and vulnerable plaques

What Are the Clinical Implications?

- These results help to advance the understanding of LXR treatment on vulnerable plaques and are promised to facilitate the eventual application of therapies targeting LXR α .
- Taking the dumbness of LXR β and the adverse effects of LXR α in treating vulnerable plaques into consideration, lesional drug delivery might be preferable to systemic activation of LXR α .

Nonstandard Abbreviations and Acronyms

7-KC	7-ketocholesterol
ApoE	apolipoprotein E
ER	endoplasmic reticulum
LXR	liver X receptor
UPR	unfolded protein response

Macrophages are the key drivers of atherothrombotic processes. Their apoptosis and efferocytosis (the clearance of apoptotic cells) play pivotal roles in determining the rupture or regression fate of plaques.⁴ Excessive lipids that accumulate in endoplasmic reticulum (ER) can disturb cellular homeostasis and cause ER stress.⁵ Despite the counteracting effect of cells to mobilize the unfolded protein response (UPR), prolonged ER stress activates the CHOP pathway and leads to cell death.⁶ These apoptotic macrophages as well as red cells from intraplaque hemorrhage, which fail to be efficiently removed by phagocytes, facilitate the necrotic core formation. Moreover, the nonresolving inflammatory response prevails, contributing to the loss of mechanical stability in lesions. All these events bring about fragile conditions that predispose to plaque rupture. However, the crucial factors in regulating macrophage apoptosis and the efficiency of efferocytosis are not fully known.

Liver X receptor (LXR), a member of the nuclear receptor family, is defined as a regulatory hub of

lipid metabolism and inflammation in atherosclerosis.⁷ Two isotypes of LXRs, LXR α and LXR β , have similar but not identical properties. Ways of activating LXR vary, compared with its natural sterol ligands; nonsterol agonists like GW3965 have a more potent effect on LXR target genes.⁸ Our previous studies have revealed that LXR protects cardiomyocytes against myocardial ischemia/reperfusion injury and postmyocardial infarction remodeling, mainly through LXR α .^{9,10} Then, questions that need to be asked are as follows: (1) What effects can LXR exert on vulnerable plaques before the fatal cardiac ischemia happens? (2) Does LXR have a protective role in ER stress-induced macrophage apoptosis and impaired apoptotic cell clearance? (3) Which isotype of LXR is responsible for the protection?

In the present study, using a mice model of rupture-prone plaques, we seek to figure out the impacts of LXR activation on vulnerable plaques, and the role of LXR α on macrophage apoptosis and efferocytosis in response to ER stress in vitro/in vivo. These efforts may advance our knowledge of LXR from a therapeutic perspective.

METHODS

The authors declare that all supporting data are available within the article and its online supplementary files.

Animal Experiment

The animal protocol was approved by the institutional ethics committee of Renji Hospital (RJ2018-1030), and the study was performed according to the National Institutes of Health *Guide for the Care and Use of Laboratory Animals*.

ApoE^{-/-} mice (20–25 g) on a C57BL/6 background (GemPharmatech, China) were randomly enrolled into 3 groups: baseline, vehicle, and GW3965. All 3 groups received surgery, as previously described.^{11–14} In brief, 8-week-old male ApoE^{-/-} mice underwent the branch ligation of the left common carotid artery, with the left superior thyroid artery remaining intact, and the left renal artery was constricted using a pin gauge (0.12 mm in diameter) to preserve renal perfusion. Anesthesia was performed via an intraperitoneal injection of pentobarbital sodium (50 mg/kg), and surface anesthetic agent lidocaine (dilute to 0.5%) was adopted locally before making a surgical incision, or before final skin closure. Levels of anesthesia were assessed by pedal reflex (firm toe pinch), and respiratory rates were monitored at 15-minute intervals. Then, mice were fed a high-fat diet (40 kcal% fat, 1.25% cholesterol, and 0.5% cholic acid; Research Diets) for 4 weeks. Magnetic

resonance imaging (MRI) scans were applied every 2 weeks. The first assay happened right after the surgery procedure. At 4 weeks after the surgery, the mice in the baseline group were euthanized. The GW3965 and vehicle groups were administered GW3965 (10 mg/kg per day) and 5% dimethyl sulfoxide in PBS, respectively, for another 4 weeks by intraperitoneal injection. LXR α -deficient mice, generously provided by Dr Ancai Yuan (Shanghai Jiao Tong University), were intercrossed with ApoE $^{-/-}$ mice to generate LXR $\alpha^{-/-}$ ApoE $^{-/-}$ mice. Key resources are listed in Table S1.

MRI Scans

The 7.0-T MRI (Bruker, Germany) was applied for in vivo lesion detection. A gas anesthesia machine with an oxygen source and a precision vaporizer was adopted. Mice were anesthetized by isoflurane inhalation (3% for induction, and 1.5% for maintenance) and placed in a prone position. Three MRI sequences (PD, T2, and T2 star) were applied. Detailed parameters are available in Data S1.

Tissue Collection

Mice were anesthetized with sustained isoflurane inhalation (3%), and blood was collected by cardiac puncture after rib removal. Freshly obtained EDTA blood was used to measure complete blood counts using the XT-2000i hematology analyzer (Sysmex, Germany). To obtain plasma, blood was placed for 15 minutes at room temperature, then centrifuged at 1500g for 15 minutes at 4°C. Plasma levels of total cholesterol and triglycerides were measured with Hitachi 7180 autoanalyzer (Hitachi High-Technologies Corp, Japan). Exsanguination was used as a means of euthanasia in this condition. Detailed method descriptions are available in Data S1.

Histological Staining of Murine Left Common Carotid Artery

These experiments were performed as described,¹⁵ and details are shown in Data S1.

Immunofluorescence

These experiments were performed as described,¹⁵ and details are shown in Data S1.

In Situ Lesional Apoptosis and Efferocytosis Assay

Detailed method descriptions are available in Data S1.

In Vivo Efferocytosis Assay

Detailed method descriptions are available in Data S1.

Cell Culture

Raw 264.7 (mouse macrophage) cells were maintained in DMEM (Gibco), and Jurkat (human T-lymphocyte) cells were maintained in Roswell Park Memorial Institute 1640 medium (Gibco), supplemented with 10% (vol/vol) fetal bovine serum (Gibco) and 10 U/mL penicillin and 100 mg/mL streptomycin (Gibco). Cells were cultured in a humidified CO₂ incubator at 37°C. Cells were treated with 7-ketocholesterol (7-KC; Sigma-Aldrich) and GW3965 (MedChemExpress, China), as indicated. 7-KC was dissolved in ethanol, and GW3965 was dissolved in dimethyl sulfoxide.

Primary Macrophage Experiment

Primary peritoneal macrophages from LXR α knockout and LXR β knockout mice were obtained. In brief, 1 mL of 4% Brewer thioglycollate medium (Sigma-Aldrich) was injected into the peritoneal cavity of each mouse. The mice were euthanized with anesthetic overdose after 4 days of stimulation. Peritoneal exudate cells were obtained by rinsing the peritoneal cavity with 10 mL of cold PBS 3 times in a sterile condition, centrifuged at 200g for 10 minutes at 4°C, and plated in culture media (DMEM containing 10% fetal bovine serum). After 4 hours, cells were washed with warm PBS, and new culture medium was added.

Real-Time Quantitative Polymerase Chain Reaction

Detailed method descriptions are available in Data S1.

Western Blotting Assay

Detailed method descriptions are available in Data S1.

Macrophage Apoptosis Experiment

Detailed method descriptions are available in Data S1.

In Vitro Efferocytosis Assay

Detailed method descriptions are available in Data S1.

Statistical Analysis

Data were analyzed with GraphPad Prism (Version 7.0). Normality was tested with the Shapiro-Wilk normality tests. Normally distributed variables are expressed as mean \pm SEM. The incidence of plaque rupture was evaluated via χ^2 test with Yates' correction. We used Student *t* test to assess the effects of parameters between 2 different groups (unpaired test). 2-way repeated-measures ANOVA, followed by Bonferroni multiple-comparisons test; 1-way ANOVA, followed by Dunnett multiple-comparisons test or Tukey multiple-comparisons test; and 2-way ANOVA, followed by Tukey multiple-comparisons test, were

made as appropriate. The Pearson correlation coefficient was done as appropriate. $P < 0.05$ was considered as being statistically significant.

RESULTS

The Vulnerable Plaque Is Established at 4 Weeks After Surgery in the Left Common Carotid Artery

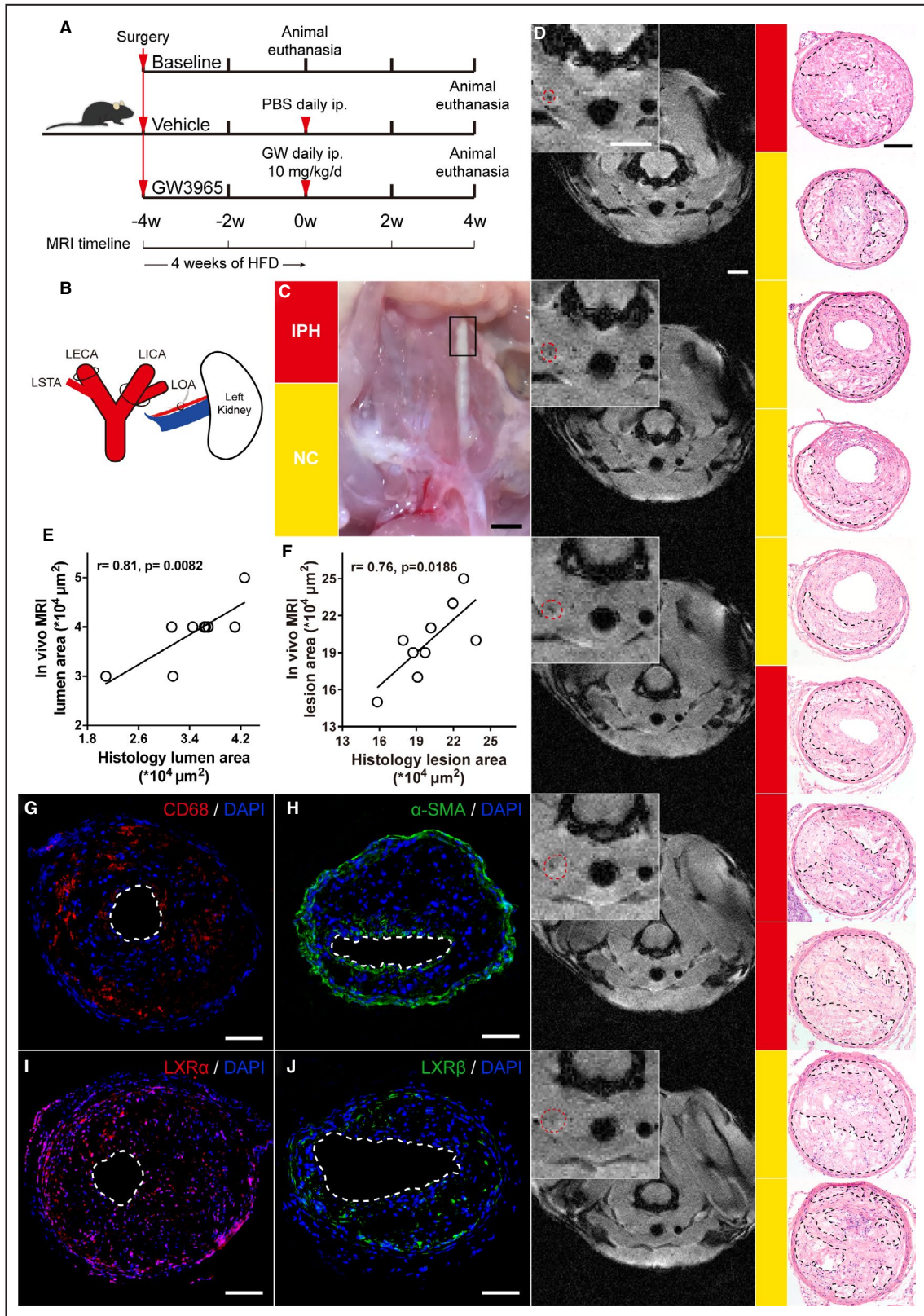
To establish vulnerable plaques in the left common carotid artery, we adopted artery ligations and fed the ApoE^{-/-} mice with high-fat diets (Figure 1A and 1B). At 4 weeks after surgery, mice in the baseline group were examined using MRI scans and hematoxylin and eosin staining. To make it comparable, the first section in each method was selected from the level of the carotid artery bifurcation. Every 2 serial sections were spaced 500 μm in MRI, and 250 μm in the histological staining. These parameters assured us that 1 MRI picture corresponded to 2 hematoxylin and eosin images. The 2500- μm range of left common carotid artery was presented in line (Figure 1D). The black box in Figure 1C denoted the corresponding gross picture. As we could see, features like intraplaque hemorrhage and necrotic core formation, which were highlighted, occurred at a high frequency. We also found that macrophages prevailed in the subendothelial area, and smooth muscle cells migrated to the intima region (Figure 1G and 1H). Interestingly, LXR α protein was highly expressed in the lesion area, whereas the expression of LXR β scattered in the subintimal area close to media (Figure 1I and 1J). More important, the Pearson correlation (Figure 1E and 1F) demonstrated that MRI is a valuable tool to trace individual plaque growth; the correlation between in vivo MRI lumen area and histology lumen area is high ($r = 0.81$; $P = 0.0082$); and either is lesion area ($r = 0.76$; $P = 0.0186$). The preexisting unstable plaque was established to explore drug effects in vulnerable plaque experiments.

Activating LXR Reduces Vulnerable Features and Prevents Plaque Rupture in Preexisting Unstable Lesions

Confirming the existence of unstable plaques, mice were administered GW3965 (an agonist of LXR) or vehicle solution daily by intraperitoneal injection for another 4 weeks. Longitudinal MRI scans were applied to each mouse. As we collected images from 3 MRI sequences (PD, T2, and T2 star), the plaque could be traced and outlined in an integrated and dynamic way (Figure S1A). On 4 weeks of GW3965 administration, the arterial outward remodeling was ameliorated (vehicle 4 weeks versus GW3965 4 weeks: $26.17 \pm 0.98 \times 10^4$ versus $13.83 \pm 0.40 \times 10^4$ μm^2 ; $P < 0.0001$), with the wall area decreased ($27 \pm 1.03 \times 10^4$ versus $19 \pm 0.37 \times 10^4$ μm^2 ; $P < 0.0001$), whereas the lumen area was increased ($0.83 \pm 0.31 \times 10^4$ versus $5.17 \pm 0.31 \times 10^4$ μm^2 ; $P < 0.0001$; Figure 2A through 2D). As the plaque grew, the vehicle group observed 9 of 10 greenish black left common carotid arteries, whereas the GW3965 group had only 2 cases of plaque rupture (a pooled result from 2 batches of mice). Subsequent histological analysis revealed that the abnormal gross appearance was an indication of mural or occlusive thrombi with fibrous cap ruptures (Figure 2E and 2G). To get a grasp of the overall plaque burden and detailed plaque composition, consecutive carotid frozen sections were stained with hematoxylin and eosin, oil red O, and Masson trichrome staining (Figure 2F). Serial lesion area analysis indicated LXR activation had broad protection on sections calculated (Figure 2H). As a result, lesion volume and mean lesion area reduced by 52.61% and 52.01%, respectively, compared with the vehicle group (vehicle versus GW3965: $65.62 \pm 2.34 \times 10^7$ versus $31.10 \pm 2.56 \times 10^7$ μm^3 [$P < 0.0001$]; $26.32 \pm 0.96 \times 10^4$ versus $12.63 \pm 1.00 \times 10^4$ μm^2 [$P = 0.014$]; Figure 2I and 2J). Accordingly, lesional lipid deposition was reduced by 53.67% ($20.88 \pm 1.31\%$ versus $9.67 \pm 1.28\%$ of lesion area; $P = 0.004$; Figure 2K), and collagen

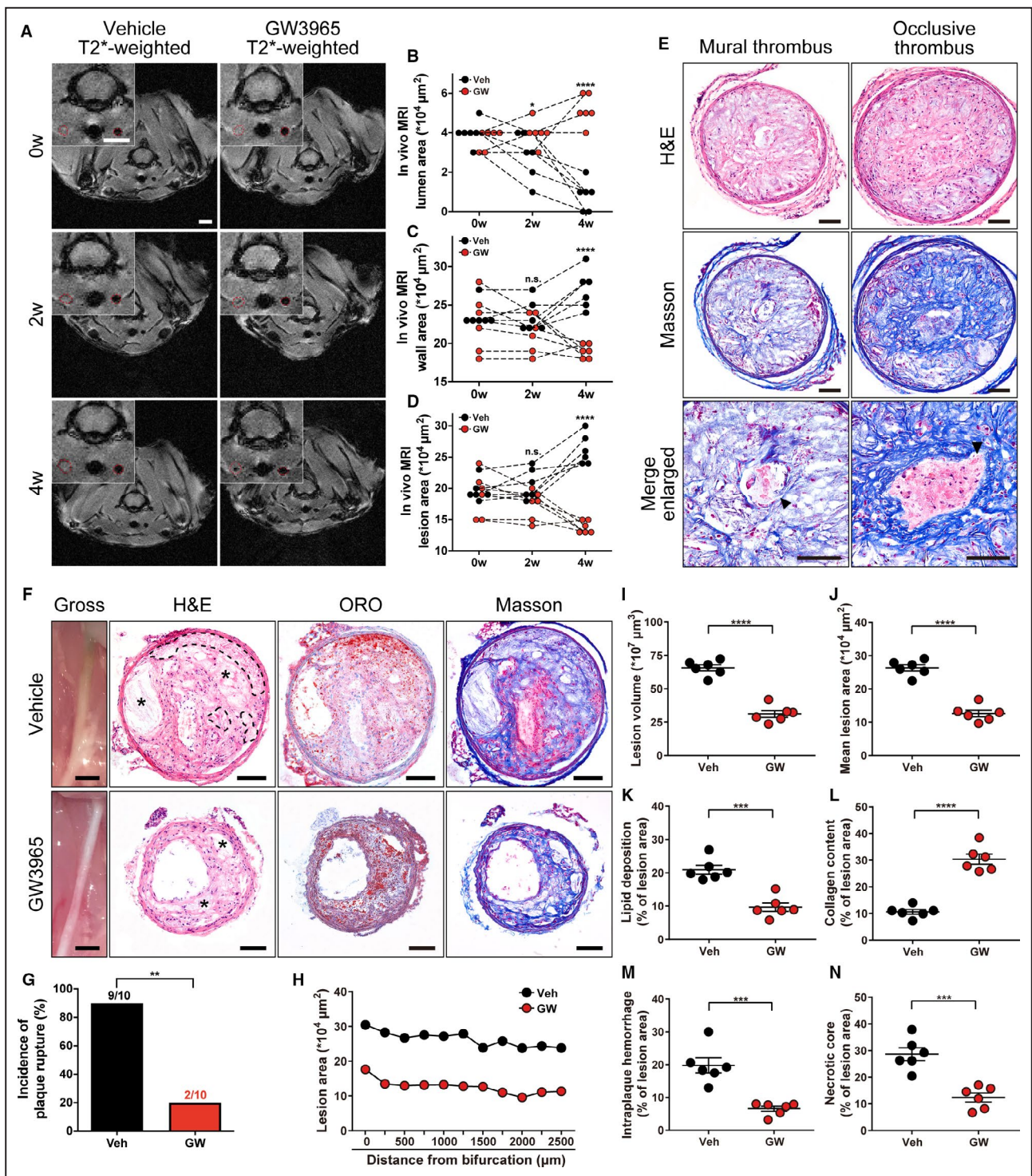
Figure 1. Vulnerable features of established atherosclerotic lesions in the left common carotid artery.

The vulnerable plaque has been established after 4 weeks (w) of ligation in the setting of hypercholesterolemia, which is confirmed by magnetic resonance imaging (MRI) scans and histological staining. **A**, The schematic of the animal experimental design. **B**, The schematic of the surgical intervention. **C**, The gross picture of the carotid artery in **D**. Rectangle denotes the 2500- μm region descending from the carotid bifurcation. Bar=2000 μm . **D**, Consecutive carotid artery sections were recorded by MRI T2 star (T2*)-weighted sequence and stained with hematoxylin and eosin (H&E). The intervals of MRI and H&E images are 500 and 250 μm , respectively. Dotted circles in red denote the artery wall. Red and yellow bars are signs of lesions dominant in intraplaque hemorrhage and necrotic core formation, respectively, and dotted lines in black nearby denote the corresponding features. Bar=1000, 1000, and 100 μm (from left to right in **D**). **E** and **F**, Graphs show correlation analysis ($n = 9$) between in vivo MRI lumen area and histology lumen area ($\times 10^4$ μm^2) (**E**), and lesion area ($\times 10^4$ μm^2) (**F**). **G** and **H**, Representative photomicrographs of carotid sections stained with an antibody against cluster of differentiation (CD) 68 (red) or α -smooth muscle actin (α -SMA) (green), and counterstained with 4',6-diamidino-2-phenylindole (DAPI) (blue). Bar=100 μm . **I** and **J**, Representative photomicrographs of carotid sections stained with an antibody against liver X receptor (LXR) α (red) or LXR β (green), and counterstained with DAPI (blue). Dotted lines denote the lumen area. Bar=100 μm . The "n" refers to the number of mice, and P values are shown as indicated (Pearson correlation coefficient for **E** and **F**). GW indicates GW3965; HFD, high-fat diet; ip., intraperitoneal injection; IPH, intraplaque hemorrhage; LECA, left external carotid artery; LICA, left internal carotid artery; LOA, left occipital artery; LSTA, left superior thyroid artery; and NC, necrotic core.



content increased by 186.42% ($10.6 \pm 0.89\%$ versus $30.36 \pm 1.92\%$ of lesion area; $P < 0.0001$; Figure 2L). Blood tests were applied at the end of the indicated

period as well, and the total cholesterol decreased (767.4 ± 56.6 versus 614.5 ± 38.6 mg/dL; $P = 0.0496$; Figure S2B), whereas triglycerides increased



(109.5±6.2 versus 148.9±8.6 mg/dL; $P=0.004$; Figure S2C). Intriguingly, a profile of less intraplaque hemorrhage detection and necrotic core formation was found (19.76±2.31% versus 6.58±0.79% of lesion area [$P<0.0001$]; 28.64±2.41% versus 12.37±1.71% of lesion area [$P<0.0001$]; Figure 2M and 2N). These results suggested that activation of LXR improved the stability of vulnerable plaques.

LXR Activation Alleviates Apoptosis and Defective Efferocytosis as Well as ER Stress in Carotid Vulnerable Plaques

The amounts of apoptotic cells and their disposal are important factors in necrotic core formation. To detect apoptosis and efferocytosis in plaque areas and investigate whether LXR activation was involved

Figure 2. Activating liver X receptor (LXR) reduces vulnerable features and prevents plaque rupture in preexisting unstable lesions.

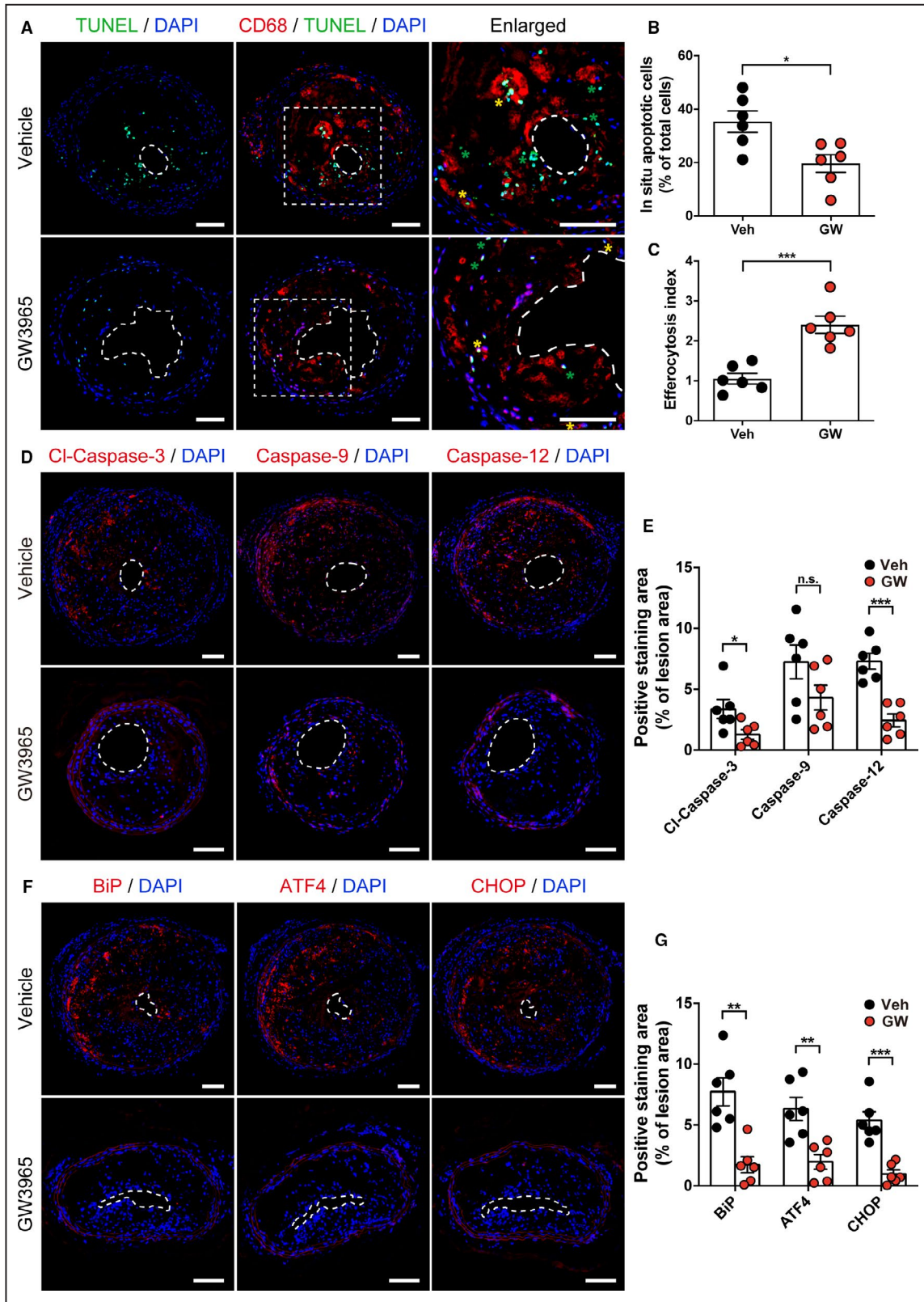
Ligand-activated LXR reduces arterial outward remodeling, intraplaque hemorrhage, and necrotic core formation in the left common carotid artery. As vulnerable plaques were established, mice were administered GW3965 (GW) (10 mg/kg per day) or 5% dimethyl sulfoxide in PBS for another 4 weeks (w) by intraperitoneal injection. **A**, Magnetic resonance imaging (MRI) T2 star (T2*)-weighted images of the carotid artery (the same level from one individual) were taken at 0, 2, and 4 weeks in the vehicle (Veh) group and the GW3965 group. Red dotted circles show the artery wall. Bar=1000 μm. **B** through **D**, Graphs show the in vivo MRI lumen area, wall area, and lesion area ($\times 10^4 \mu\text{m}^2$; n=6) measurement at the time points mentioned in **A**, when treated with GW3965 or not. **E**, Representative photomicrographs of carotid frozen sections stained with hematoxylin and eosin and Masson trichrome. Arrowheads denote fibrous cap rupture with a mural thrombus or an occlusive thrombus. Bar=100 μm. **F**, Representative gross pictures and photomicrographs of carotid frozen sections stained with hematoxylin and eosin (H&E), oil red O (ORO), and Masson trichrome. Asterisks represent the necrotic core areas, and dotted lines denote the areas of intraplaque hemorrhage. Bar=1000 (first column in **F**) and 100 μm. **G**, Graph shows the measurements of the incidence of plaque rupture (percentage; n=10). **H** through **J**, Graphs show the measurements of (1) serial lesion area ($\times 10^4 \mu\text{m}^2$; n=6); (2) lesion volume ($\times 10^7 \mu\text{m}^3$; n=6); and (3) mean lesion area ($\times 10^4 \mu\text{m}^2$; n=6). **K** and **L**, Graphs show the measurements of (1) lipid deposition (percentage of lesion area; n=6); and (2) collagen content (percentage of lesion area; n=6). **M** and **N**, Graphs show the measurements of (1) intraplaque hemorrhage (percentage of lesion area; n=6); and (2) necrotic core (percentage of lesion area; n=6). Each circle represents the average specific parameter of 8 to 11 sections in each mouse or the average lesion area of 6 mice at the indicated level in **H**. Data are presented as mean \pm SEM, and “n” refers to the number of mice. * P <0.05, ** P <0.01, *** P <0.001, **** P <0.0001 (2-way repeated-measures ANOVA, followed by Bonferroni multiple-comparisons test [**B–D**]; 2-sided χ^2 test with Yates’ correction [**G**]; 2-tailed unpaired Student t test [**I–N**]). n.s. indicates not significant.

in these processes, sections of carotid plaques were costained for DNA fragmentation with terminal deoxynucleotidyl transferase-mediated biotin-deoxyuridine triphosphate nick-end labeling (TUNEL) staining and macrophage surface marker with cluster of differentiation (CD) 68 antibody (Figure 3A). We found that the relative number of lesional apoptotic cells decreased on GW3965 intervention, compared with the vehicle group (vehicle versus GW3965: 35.35 \pm 4.02% versus 19.62 \pm 3.34% of total cells; P =0.0132; Figure 3B). Meanwhile, the percentage of apoptotic cells undergoing efferocytosis increased in plaque areas (1.05 \pm 0.13 versus 2.40 \pm 0.22; P =0.0003; Figure 3C). We then conducted flow cytometry assays evaluating peritoneal uptake of labeled apoptotic cells. The GW3965 group showed superior phagocytic capacity to the vehicle group (42.57 \pm 9.44% versus 81.90 \pm 2.54% of F4/80⁺ cells; P =0.0158; Figure S3A and S3B). Restored cell viability may enhance cell interaction and provide chances for efferocytosis. These macrophages may acquire additional antiapoptosis properties when processing cell debris. Further immunofluorescence assay on cleaved caspase-3, a canonical apoptotic effector caspase, recapitulates the above findings, referring apoptosis as a key target in the LXR treatment (3.37 \pm 0.77% versus 1.29 \pm 0.39% of lesion area; P =0.0372; Figure 3D and 3E). Then, we examined 2 apoptotic initiator caspases, mitochondrial-related caspase-9 and ER-related caspase-12, for the underlying mechanism. LXR activation profoundly reduced caspase-12 expression (7.30 \pm 0.65% versus 2.44 \pm 0.53% of lesion area; P =0.0002; Figure 3D and 3E), whereas the inhibition of caspase-9 expression was not significant (7.25 \pm 1.39% versus 4.32 \pm 1.03% of lesion area; P =0.1195; Figure 3D and 3E). As we know, ER stress could be a determinant of cell and plaque fate; we next analyzed BiP (binding-immunoglobulin protein), ATF4

(activating transcription factor 4), and CHOP (C/EBP-homologous protein) expressions within the plaque, which are recognized as ER stress markers. The vehicle group was stained positive for these 3 molecules, whereas they were barely found in the GW3965 group (7.73 \pm 1.16% versus 1.74 \pm 0.66% of lesion area [P =0.0012]; 6.32 \pm 0.95% versus 1.97 \pm 0.60% of lesion area [P =0.0032]; 5.37 \pm 0.72% versus 0.97 \pm 0.34% of lesion area [P =0.0002]; Figure 3F and 3G). Taken together, these findings showed LXR reduced apoptosis, defective efferocytosis, and ER stress in the vessel wall.

LXR Activation Inhibits 7-KC-Induced ER Stress in Macrophages

To further explore the role and potential mechanism of LXR in regulating ER stress, we did subsequent experiments focusing on macrophage apoptosis and efferocytosis in vitro. 7-KC, which belongs to the oxysterol family, is a bioactive cholesterol derivative. A recent study has shown that high plasma 7-KC levels are associated with adverse clinical outcomes in patients with stable coronary artery disease.¹⁶ In human late-stage lesions, the 7-KC abundance is only second to 27-hydroxycholesterol¹⁷; both of them are regulators of apoptosis. First, we examined UPR-related gene expressions in Raw 264.7 macrophages. Wherever in concentration-gradient or time-point experiment, CHOP expression began to increase significantly during 12 hours of 7-KC incubation at the dose of 40 μmol/L and reached its peak at 24 hours of dose 80 μmol/L (Figure S4A through S4D). Then, we adopted the combination of 40 μmol/L and 24 hours for further experiments. To investigate whether LXR plays a role in regulating ER stress in macrophages, we activated LXR with GW3965, as in the animal experiment. *Abca1*



and *Abcg1* are LXR-responsive genes involved in cholesterol efflux. With the concentration of GW3965 added up to 1 μ mol/L, the gene expressions surged (Figure S4E). UPR pathways were again examined, and

the preincubation with GW3965 for 24 hours almost offset the increased expressions of Chop, Atf4, and spliced X-box-binding protein 1 (sXBP), which were induced by 7-KC (Figure S4F). Next, an array of molecules

Figure 3. Liver X receptor (LXR) activation alleviates apoptosis and defective efferocytosis as well as endoplasmic reticulum (ER) stress in carotid vulnerable plaques.

Activating LXR through GW3965 (GW) reduces apoptosis and enhances efferocytosis in carotid arteries, and the benefits rely on modulating ER stress. **A**, Representative immunofluorescence staining of apoptosis and efferocytosis in carotid sections is shown. Macrophages were stained with an anti-cluster of differentiation (CD) 68 antibody (red), and apoptotic cells were stained with terminal deoxynucleotidyl transferase-mediated biotin-deoxyuridine triphosphate nick-end labeling (TUNEL) (green). Dotted squares (second column in **A**) indicate the corresponding part of the enlarged pictures (third column in **A**). Yellow asterisks show examples of macrophage-associated apoptotic cells, whereas green asterisks indicate free apoptotic cells. Bar=100 μ m. **B** and **C**, Graphs show the quantification of lesional apoptotic cells (percentage of total cells; n=6) (**B**) and the measurement of efferocytosis index (n=6) (**C**). The efferocytosis index is the macrophage-associated apoptotic cells/free apoptotic cells. **D**, Representative photomicrographs of carotid sections stained with an antibody against cleaved caspase-3 (Cl-Caspase-3) (red; left), caspase-9 (red; middle), or caspase-12 (red; right), and counterstained with 4',6-diamidino-2-phenylindole (DAPI) (blue). **E**, Graph shows the quantification of caspase-positive staining area (percentage of lesion area; n=6) in **D**. **F**, Representative photomicrographs of carotid sections stained with an antibody against BiP (binding-immunoglobulin protein) (red; left), ATF4 (activating transcription factor 4) (red; middle), or CHOP (C/EBP-homologous protein) (red; right), and counterstained with DAPI (blue). **G**, Graph shows the quantification of positive staining area of ER stress markers (percentage of lesion area; n=6) in **F**. Dotted lines denote the lumen areas. Data are presented as mean \pm SEM, and "n" refers to the number of mice. * P <0.05, ** P <0.01, *** P <0.001 (2-tailed unpaired Student t test [**B**, **C**, **E**, and **G**]). n.s. indicates not significant; and Veh, vehicle.

was tested by Western blotting, from the upstream ER membrane protein PRKR-like endoplasmic reticulum kinase (PERK) and inositol-requiring protein-1 α (IRE1 α) to the apoptosis effector CHOP (Figure S4G; quantification data, see Figure S5A through S5E). As we have demonstrated LXR protection on established plaques, similarly, we primed macrophages with 7-KC for 12 hours to see whether GW3965 treatment could protect irritated macrophages. The introduction of GW3965 exhibited effective protection on stressed cells at an incubating duration of 24 hours (Figure S6A and S6B). The results suggested that LXR activation silenced the decompensated UPR pathway.

The Favorable Effects of LXR Agonists on ER Stress-Related CHOP Pathway Are Lost in the Setting of Genetic Ablation of LXR α , but Not LXR β , Isotype

LXRs have 2 isotypes, LXR α and LXR β , which possess different expression patterns. We then evaluated the ability of activated LXR α or LXR β to counteract the CHOP pathway. Primary macrophages were obtained from the peritoneal cavity of isotype-specific knockout mice (Figure 4A). The expression of LXR α was detectable in LXR β -deficient macrophages, and the subsequent GW3965 intervention was sufficient to suppress 7-KC-induced CHOP pathway (BiP, P =0.0330; ATF4, P =0.0034; and CHOP, P =0.0178; Figure 4C), whereas depletion of LXR α made LXR agonists futile (Figure 4B). We conclude that GW3965 exerted ER protection mainly through LXR α .

LXR α Mediates the Effects of LXR Activation on Apoptosis Alleviation and Efferocytosis Enhancement in Macrophages

We next explore which isotype of LXRs accounts for regulating apoptosis and efferocytosis of macrophages in

vitro. For TUNEL staining, activating LXR in LXR α -deficient macrophages had no apparent impact on DNA fragmentation induced by 7-KC (7-KC versus GW3965+7-KC, 42.70 \pm 4.01% versus 36.32 \pm 3.58% of total cells; P =0.3998; Figure 5A and 5B). As mentioned above, caspase-3 activation is a classic biological marker for apoptosis, and full-length caspase-3 is cleaved into a 17-kDa fragment during apoptosis. Therefore, we examined the protein levels of cleaved caspase-3. GW3965 intervention did not reduce the protein expression of cleaved caspase-3 in the setting of genetic ablation of LXR α (P =0.9998; Figure 5C; quantification data, see Figure S5G). However, LXR activation in wild-type controls or with LXR β deficiency was able to alleviate macrophage apoptosis in TUNEL staining and in Western blotting assay (Figures S7A through S7C and S8A through S8C). The lipid overloading stress is decisive not only in the cell fate but also in the ability of macrophages to remove apoptotic cells. Apoptotic cells were generated by a UV irradiating on Jurkat cells. Fluorescein-labeled apoptotic cells were added to cell culture media of macrophages. Using a combination of bright-field and fluorescent-field or flow cytometry analysis, efferocytosis was evaluated and depicted as the association between macrophages and apoptotic cells. The results revealed that phagocytosis decreased in 7-KC stimulation (Figure S7D through S7G). LXR α knockout, but not LXR β knockout, damaged the capability of LXR activation to reverse the efferocytosis impairment (10.01 \pm 0.70% versus 11.86 \pm 1.27% [P =0.8686]; 8.51 \pm 0.55% versus 9.04 \pm 0.68% [P =0.9797]; Figure 5D through 5G; Figure S8D through S8G). In sum, LXR α mediated the protective effects of LXR activation on fixing macrophage malfunction, whereas LXR β was dispensable.

LXR α Knockout Renders GW3965 Invalid in Reducing Plaque Vulnerability

Prompted by our in vitro data, we generated LXR α ^{-/-}ApoE^{-/-} mice to further evaluate if LXR α plays a crucial role in stabilizing plaques. First of all, LXR α

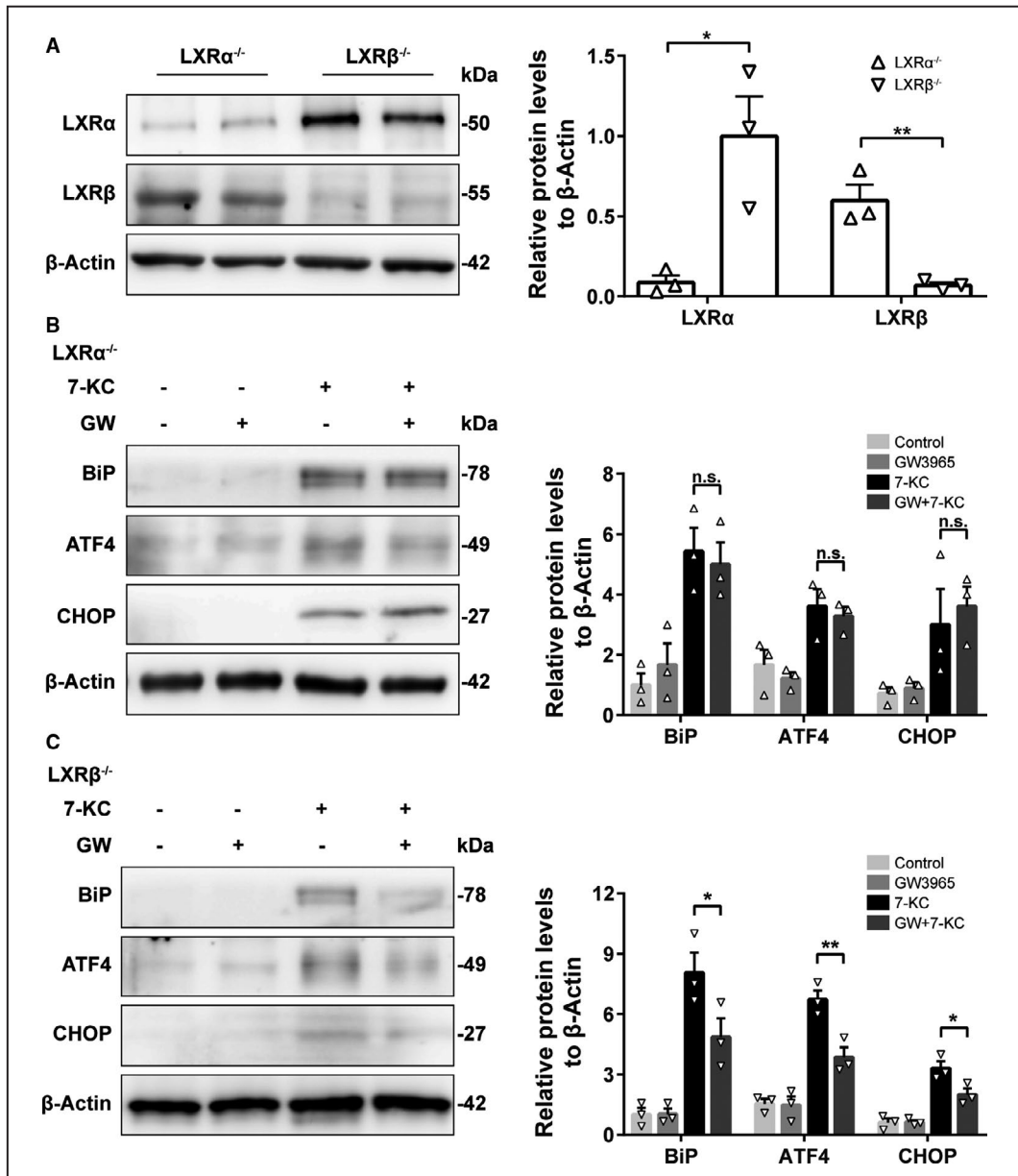
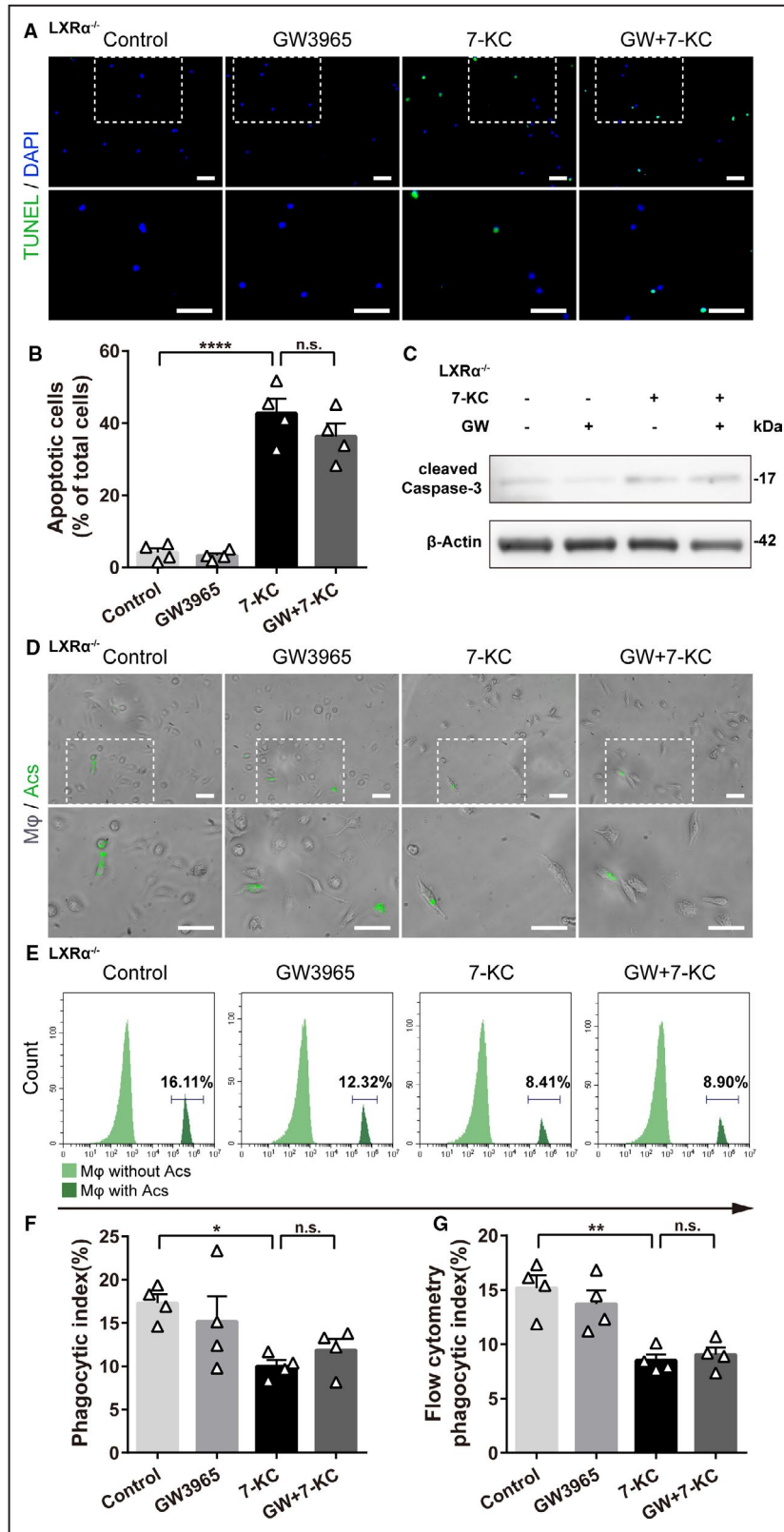


Figure 4. The favorable effects of liver X receptor (LXR) agonists on endoplasmic reticulum (ER) stress-related CHOP pathway are lost in the setting of genetic ablation of LXR α , but not LXR β . Peritoneal macrophages from LXR α knockout or LXR β knockout mice were isolated and treated as indicated. Then, proteins were collected for the Western blotting assay (n=3). **A**, Isotype-specific gene knockout in peritoneal exudate cells was confirmed by Western blotting (n=3). The graph shows the relative protein levels to β -actin. **B** and **C**, GW3965 (GW)-activated LXR in LXR α -deficient macrophage had minor effects on 7-ketocholesterol (7-KC)-induced C/EBP-homologous protein (CHOP) pathway, including binding-immunoglobulin protein (BiP), activating transcription factor 4 (ATF4), and CHOP protein expressions, whereas ligand activation of LXR in the absence of LXR β is sufficient to suppress CHOP-mediated ER stress. Graphs show the relative protein levels to β -actin. Data are presented as mean \pm SEM, and “n” refers to the number of independent experiments taken. * P <0.05, ** P <0.01 (2-tailed unpaired Student t test [A], 1-way ANOVA, followed by the Tukey multiple-comparisons test [B and C]). n.s. indicates not significant.

protein expression was rarely found in the vessel wall of LXR $\alpha^{-/-}$ ApoE $^{-/-}$ mice (Figure S9A). After 4 weeks of plaque progression, only 1 of 9 individuals in the LXR $\alpha^{-/-}$ ApoE $^{-/-}$ group and none of the ApoE $^{-/-}$ mice had a trace of plaque rupture (Figure S9B), and no mouse died in both groups.

Compared with ApoE $^{-/-}$ mice using histological methods (Figure S9C), mice of additional general knockout of LXR α might acquire more diffused and bigger plaque alongside the vessel bed (Figure S9D through S9F), with lipid deposition increased, and collagen content was not evidently



deteriorated (Figure S9G and S9H). At the time point of 4 weeks, intraplaque hemorrhage and necrotic core areas were not significantly changed (Figure S9I and S9J). Leaving the plaque in LXR $\alpha^{-/-}$ ApoE $^{-/-}$ mice to grow, each

group had 2 mice that died (death cases were excluded from the further statistical evaluation; Figure 6A). Evidence of occlusive thrombosis was found in the autopsy. The plaques progressed to a more advanced stage, and each

Figure 5. Genetic ablation of liver X receptor (LXR) α blunts the beneficial effects of LXR activation on macrophage apoptosis and defective efferocytosis.

GW3965 (GW) was added to 7-ketocholesterol (7-KC)-flamed peritoneal macrophages from LXR $\alpha^{-/-}$ mice. **A** and **B**, Terminal deoxynucleotidyl transferase-mediated biotin–deoxyuridine triphosphate nick-end labeling (TUNEL) staining (n=4) of macrophage apoptosis was performed in different treatment conditions described previously. Representative photomicrographs show that LXR agonists in LXR α -deficient macrophages scarcely reduced TUNEL-positive cells (green) induced by 7-KC. Dotted squares (first row in **A**) indicate the corresponding part of enlarged pictures (second row in **A**). Bar=100 μ m. The graph shows apoptotic cell measurements. **C**, Western blotting of cleaved caspase-3 protein expression (n=3) was also adopted to access the protective effects of LXR activation on apoptosis. **D** and **E**, In vitro efferocytosis assay (n=4) was conducted using peritoneal macrophages from LXR α knockout mice. Apoptotic cells (green) that colocalized with macrophages in the bright field were reckoned as effective efferocytosis. Dotted squares (first row in **D**) indicate the corresponding part of the enlarged pictures (second row in **D**). Bar=100 μ m. Representative photomicrographs show that more free macrophages (apoptotic cells without macrophage association) were observed on 7-KC stimulation, and benefits of LXR treatment were rarely found. Flow cytometry analysis (n=4) was adopted as well. **F** and **G**, Graphs show the phagocytic index measurements. The phagocytic index is defined as the ratio of apoptotic cell-associated macrophages/total cells. Data are presented as mean \pm SEM, and “n” refers to the number of independent experiments taken. * P <0.05, ** P <0.01, **** P <0.0001 (1-way ANOVA, followed by the Tukey multiple-comparisons test [**B**, **F**, and **G**]). AcS indicates apoptotic cells; DAPI, 4',6-diamidino-2-phenylindole; M ϕ , macrophages; and n.s., not significant.

individual in the vehicle group exhibited signs of plaque rupture. When it comes to GW3965 intervention, there were still 8 of 9 mice that experienced plaque rupture (LXR $\alpha^{-/-}$ ApoE $^{-/-}$ vehicle versus LXR $\alpha^{-/-}$ ApoE $^{-/-}$ GW3965: 9/9 versus 8/9; P >0.9999; Figure 6B). Specifically, plaque burden was similar in these 2 groups ($73.98\pm 2.90\times 10^7$ versus $73.27\pm 4.52\times 10^7$ μm^3 [$P=0.9989$]; $29.72\pm 1.19\times 10^4$ versus $29.57\pm 1.79\times 10^4$ μm^2 [$P=0.9998$]; Figure 6E and 6F); neither lipid/collagen profile ($23.16\pm 1.77\%$ versus $21.59\pm 1.73\%$ of lesion area [$P=0.8823$]; $13.84\pm 1.51\%$ versus $14.81\pm 1.42\%$ of lesion area [$P=0.9644$]; Figure 6G and 6H) nor vulnerable features of intraplaque hemorrhage or necrotic core showed noticeable differences ($19.35\pm 1.37\%$ versus $19.54\pm 1.13\%$ of lesion area [$P=0.9997$]; $30.93\pm 2.19\%$ versus $29.77\pm 2.14\%$ of lesion area [$P=0.9713$]; Figure 6I and 6J). However, when compared with GW3965 group in ApoE $^{-/-}$ mice, the protection of LXR activation in LXR $\alpha^{-/-}$ ApoE $^{-/-}$ mice was largely damaged (ApoE $^{-/-}$ GW3965 versus LXR $\alpha^{-/-}$ ApoE $^{-/-}$ GW3965: $40.43\pm 1.89\times 10^7$ versus $73.27\pm 4.52\times 10^7$ μm^3 [$P=0.0001$]; $16.28\pm 0.78\times 10^4$ versus $29.57\pm 1.79\times 10^4$ μm^2 [$P<0.0001$] [Figure 6E and 6F]; $11.06\pm 1.35\%$ versus $21.59\pm 1.73\%$ of lesion area [$P=0.0029$]; $25.73\pm 2.15\%$ versus $14.81\pm 1.42\%$ of lesion area [$P=0.0013$] [Figure 6G and 6H]; $7.27\pm 0.76\%$ versus $19.54\pm 1.13\%$ of lesion area [$P=0.0004$]; $14.78\pm 1.36\%$ versus $29.77\pm 2.14\%$ of lesion area [$P=0.0007$] [Figure 6I and 6J]). On the whole, silencing LXR α impairs plaque protection originated from LXR activation.

Protective Effects of LXR Activation Against Lesional Macrophage Apoptosis, Impaired Efferocytosis, and Excessive ER Stress Are Abrogated in LXR α ; ApoE $^{-/-}$ Mice

We next scrutinize biological processes in the plaque area (Figure 7A through 7C). Although no distinguishing differences in vulnerable features were found, macrophage infiltration increased in

LXR $\alpha^{-/-}$ ApoE $^{-/-}$ mice at 4 weeks compared with ApoE $^{-/-}$ mice (Figure S10D). Intriguingly, lesional macrophage apoptosis and efferocytosis varied little (Figure S10E and S10F), whereas cleaved caspase-3-positive macrophages (Figure S10G) and CHOP-positive macrophages increased (Figure S10H). At 8 weeks, ER stress prevailed in plaque areas in LXR $\alpha^{-/-}$ ApoE $^{-/-}$ mice, and administration of GW3965 shows low potency to alleviate macrophage abundance (LXR $\alpha^{-/-}$ ApoE $^{-/-}$ vehicle versus LXR $\alpha^{-/-}$ ApoE $^{-/-}$ GW3965: $82.62\pm 2.67\%$ versus $82.4\pm 2.12\%$ of total cells; $P=0.9999$; Figure 7D), apoptosis ($46.78\pm 2.83\%$ versus $45.65\pm 3.81\%$ of CD68 $^{+}$ cells; $P=0.9939$; Figure 7E), defective efferocytosis (0.95 ± 0.11 versus 1.02 ± 0.15 ; $P=0.988$; Figure 7F), cleaved caspase-3 expression ($56.16\pm 3.82\%$ versus $53.01\pm 2.34\%$ of CD68 $^{+}$ cells; $P=0.8664$; Figure 7G), and CHOP expression ($16.52\pm 1.34\%$ versus $16.11\pm 1.27\%$ of CD68 $^{+}$ cells; $P=0.9944$; Figure 7H). When compared with GW3965 group in ApoE $^{-/-}$ mice, the above-mentioned benefits of LXR activation were impaired in LXR $\alpha^{-/-}$ ApoE $^{-/-}$ mice (ApoE $^{-/-}$ GW3965 versus LXR $\alpha^{-/-}$ ApoE $^{-/-}$ GW3965: $67.70\pm 2.33\%$ versus $82.4\pm 2.12\%$ of total cells [$P=0.0044$] [Figure 7D]; $22.48\pm 2.97\%$ versus $45.65\pm 3.81\%$ of CD68 $^{+}$ cells [$P=0.0015$] [Figure 7E]; 2.66 ± 0.30 versus 1.02 ± 0.15 [$P<0.0001$] [Figure 7F]; $26.18\pm 3.03\%$ versus $53.01\pm 2.34\%$ of CD68 $^{+}$ cells [$P=0.0001$] [Figure 7G]; $7.90\pm 1.03\%$ versus $16.11\pm 1.27\%$ of CD68 $^{+}$ cells [$P=0.0026$] [Figure 7H]). These data collectively demonstrate the importance of LXR α throughout the formation and rupture of vulnerable plaques.

DISCUSSION

In the current study, we assessed LXR protection on mice vulnerable plaques and lipid-stressed macrophages. We found that LXR activation alleviated

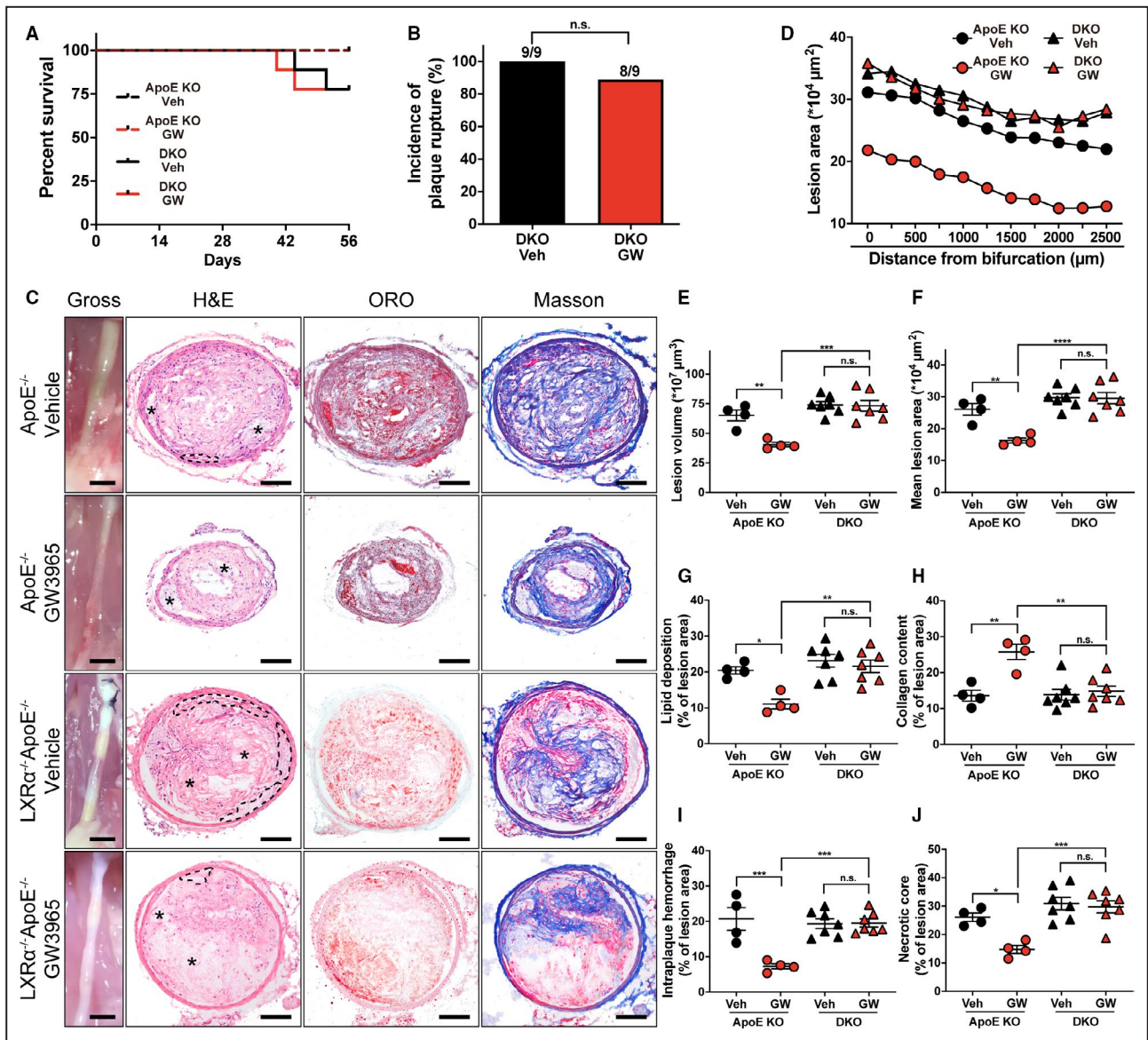
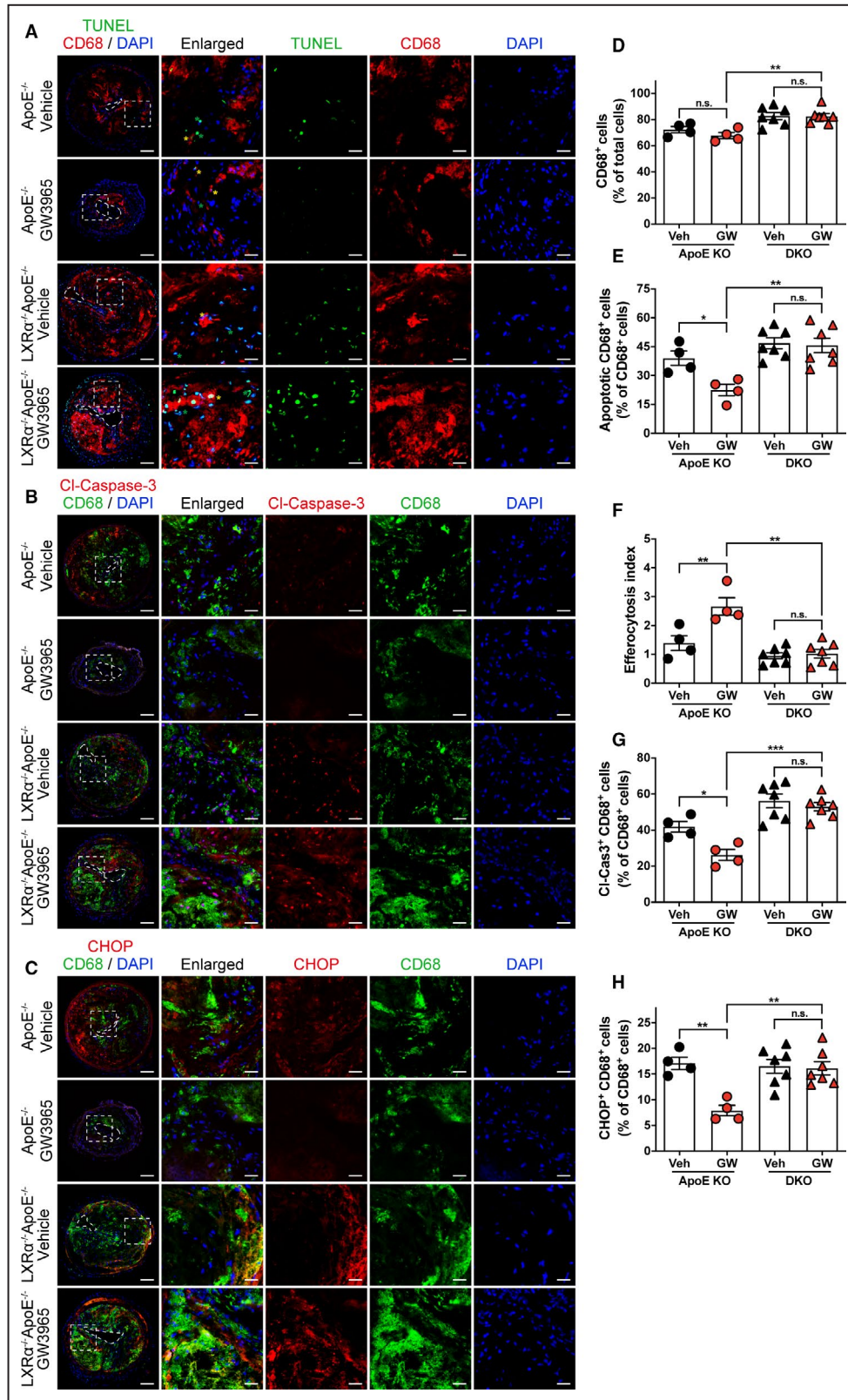


Figure 6. Liver X receptor (LXR) α knockout renders GW3965 (GW) invalid in reducing plaque vulnerability. LXR $\alpha^{-/-}$ apolipoprotein E (ApoE) $^{-/-}$ mice were generated to further detect vulnerable features in our rupture-prone model when losing LXR α functions. Deletion of the isotype LXR α exacerbates plaque progression and blunts plaque stabilization benefits exerted by LXR agonist administration. **A**, Graph shows the survival curves of 4 groups. **B**, Graph shows the measurements of the incidence of plaque rupture (percentage). **C**, Representative gross pictures and photomicrographs of carotid frozen sections stained with hematoxylin and eosin (H&E), oil red O (ORO), and Masson trichrome. Asterisks represent the necrotic core areas, and dotted lines denote the areas of intraplaque hemorrhage. Bar=1000 (first column in **C**) and 100 μ m. **D** through **F**, Graphs show the measurements of (1) serial lesion area ($\times 10^4 \mu\text{m}^2$); (2) lesion volume ($\times 10^7 \mu\text{m}^3$); and (3) mean lesion area ($\times 10^4 \mu\text{m}^2$). **G** and **H**, Graphs show the measurements of (1) lipid deposition (percentage of lesion area); and (2) collagen content (percentage of lesion area). **I** and **J**, Graphs show the measurements of (1) intraplaque hemorrhage (percentage of lesion area); and (2) necrotic core (percentage of lesion area). For **A** through **J**, n=4 in both ApoE $^{-/-}$ vehicle (Veh) and ApoE $^{-/-}$ GW3965 groups; n=7 in both LXR $\alpha^{-/-}$ ApoE $^{-/-}$ vehicle and LXR $\alpha^{-/-}$ ApoE $^{-/-}$ GW3965 groups. Each circle/triangle represents the average specific parameter of 8 to 11 sections in each mouse or the average lesion area of 4 or 7 mice at the indicated level in **D**. Data are presented as mean \pm SEM, and “n” refers to the number of mice. * $P < 0.05$, ** $P < 0.01$, *** $P < 0.001$, **** $P < 0.0001$ (2-sided χ^2 test with Yates’ correction [**B**]; 2-way ANOVA, followed by the Tukey multiple-comparisons test [**E** through **J**]). ApoE KO indicates ApoE $^{-/-}$; DKO, LXR $\alpha^{-/-}$ ApoE $^{-/-}$; and n.s., not significant.

vulnerable characteristics, such as arterial outward remodeling, intraplaque hemorrhage, and necrotic core formation, mainly through LXR α . Consequently, plaques acquire resistance to rupture.

On the basis of our previous work on this nuclear receptor as well as the mouse model of plaque rupture, we supposed LXR might exert focal protection apart from its lipid-lowering effect, which is important



to stabilize rupture-prone plaques, as the late-stage lesions not only experienced a poor systemic lipid profile but also the local inflammation and stress. Herein, we modified a well-described mice model of plaque

rupture to get vulnerable plaques.^{11,12,18,19} Endogenous renovascular hypertension combined with carotid low shear stress was achieved by artery ligations. Then, a high-fat diet was added (to accelerate the progression

Figure 7. Protective effects of liver X receptor (LXR) activation against lesional macrophage apoptosis, impaired efferocytosis, and excessive endoplasmic reticulum stress were abrogated in LXR α ^{-/-} apolipoprotein E (ApoE)^{-/-} mice.

Macrophage viability and function in vulnerable plaques remain defective in the case of LXR α gene ablation, even when supplemented with LXR pan-agonist GW3965 (GW). **A**, Representative immunofluorescence staining of macrophage apoptosis and efferocytosis in carotid sections is shown. Macrophages were stained with an anti-cluster of differentiation (CD) 68 antibody (red), and apoptotic cells were stained with terminal deoxynucleotidyl transferase-mediated biotin-deoxyuridine triphosphate nick-end labeling (TUNEL) (green). Yellow asterisks show examples of macrophage-associated apoptotic cells, whereas green asterisks indicate free apoptotic cells. Bar=100 μ m. **B**, Representative photomicrographs of carotid sections stained with antibodies against cleaved caspase-3 (Cl-Caspase-3) (red) and CD68 (green), and counterstained with 4',6-diamidino-2-phenylindole (DAPI) (blue). Bar=100 μ m. **C**, Representative photomicrographs of carotid sections stained with antibodies against C/EBP-homologous protein (CHOP) (red) and CD68 (green), and counterstained with DAPI (blue). Dotted squares (second column in **A** through **C**) indicate the corresponding part of the enlarged pictures (third column in **A** through **C**). Bar=100 μ m. **D**, Graph shows the quantification of CD68⁺ cells (percentage of total cells). **E** and **F**, Graphs show the quantification of lesional apoptotic CD68⁺ cells (percentage of CD68⁺ cells) (**E**) and the measurement of efferocytosis index (**F**). The efferocytosis index is the macrophage-associated apoptotic cells/free apoptotic cells. **G**, Graph shows the quantification of cleaved caspase3 (Cl-Cas3)⁺CD68⁺ cells (percentage of CD68⁺ cells). **H**, Graph shows the quantification of CHOP⁺CD68⁺ cells (percentage of CD68⁺ cells). Dotted lines denote the lumen areas. For **D** through **H**, n=4 in both ApoE^{-/-} vehicle (Veh) and ApoE^{-/-} GW3965 groups; n=7 in both LXR α ^{-/-}ApoE^{-/-} vehicle and LXR α ^{-/-}ApoE^{-/-} GW3965 groups. Data are presented as mean \pm SEM, and "n" refers to the number of mice. *P<0.05, **P<0.01, ***P<0.001 (2-way ANOVA, followed by the Tukey multiple-comparisons test [**D-H**]). ApoE KO indicates ApoE^{-/-}; DKO, LXR α ^{-/-}ApoE^{-/-}; and n.s., not significant.

of early-phase plaques to a vulnerable stage), so that vulnerable plaques that originally required 8 weeks to form basically have the relevant characteristics at 4 weeks (except for the low incidence of rupture), as shown in Figure 1. In the real-world practice, patients stratified as high-risk individuals with atherosclerotic cardiovascular disease were told to stop excessive fat intake and start lipid-lowering therapy. Our pilot study revealed that plaques with sustained lesional lipid burden (continued high-fat diet supply) commonly coexist with large necrotic core areas. They together result in reduced cell number. The low cellularity may cause difficulties in detecting other parameters of interest (ie, ER stress, apoptosis, and efferocytosis) in the mechanistical exploration. Thus, we adopted a high-fat diet retraction strategy as the drug intervention period began. More important, after 8 weeks of plaque progression (high-fat diets are retracted during the last 4 weeks), short-term events happen in the vehicle group and are concomitant with evident phenotype anomalies. We thus obtained established plaques at 4 weeks to facilitate our drug intervention for vulnerable plaque experiments.

LXRs have 2 isotypes, LXR α and LXR β , that are encoded by Nr1h3 and Nr1h2, respectively. LXR α is expressed in metabolically active tissues or cells, like the liver, intestines, and macrophages, whereas LXR β is ubiquitously expressed.²⁰ Previous work has shown LXR α protein is highly expressed in human lesional foam cells positive for CD68.²¹ In our study, evaluation of LXR α and LXR β proteins in plaque areas provided some interesting information; LXR α expression diffused in the lesion area, whereas LXR β was mainly located in the peri-intimal region (Figure 1). Lesional expression of LXR proteins was a prerequisite of LXR activation in vivo, whereas distinct expression pattern might indicate their differential roles in plaque progression. On 4 weeks of treatment on unstable lesions by

LXR agonist GW3965, the progression of plaque burden and lipid deposition were retarded. In contrast, the collagen content was elevated. More important, activating LXR alleviated intraplaque hemorrhage and necrotic core formation. At last, the incidence of plaque rupture in the GW3965 group decreased to a low level (Figure 2).

As a result of lacking plaque rupture mice model, scientific evidence of LXR treatment on clinically relevant plaques is insufficient. Our current study may shed some light on this field. Previous studies have shown that LXR agonists retard lesion growth in ApoE knockout, low-density lipoprotein receptor knockout, or ApoE*3-Leiden mice mainly through lipid modulation.^{8,22,23} In these experiments, efficient reverse cholesterol transport and elevated high-density lipoprotein were detected.²⁴ Despite the atheroprotective effects, severe hypertriglyceridemia and hepatic steatosis are barriers to their clinical use.^{20,25} Treatment on macrophage LXR of target organs may be a decent solution, as macrophage overexpression of LXR α ameliorates atherosclerosis as well as hypertriglyceridemia,^{26,27} whereas deletion of macrophage LXR brings harm.^{7,28} In addition, activated LXR β is enough to provide resistance to early lesion progression in the setting of hypercholesterolemia,²⁹ although LXR α is required for a robust response to LXR ligands.³⁰ More nonlipid effects of LXR have been revealed. LXR agonists can still be atheroprotective when lacking ABCA1/G1 in macrophages, mainly through the transrepression of inflammatory genes.³¹ In a regression model, aortic arches from ApoE^{-/-} mice with bone marrow deficiency of LXR α or LXR β were transplanted into wild-type recipients. Plaques from both LXR α -deficient mice and LXR β -deficient ApoE^{-/-} mice exhibited impaired regression.³² Intriguingly, a study performed in New Zealand white rabbits has shown that LXR agonist LXR-623 exerts significant effects on plaque regression in combination

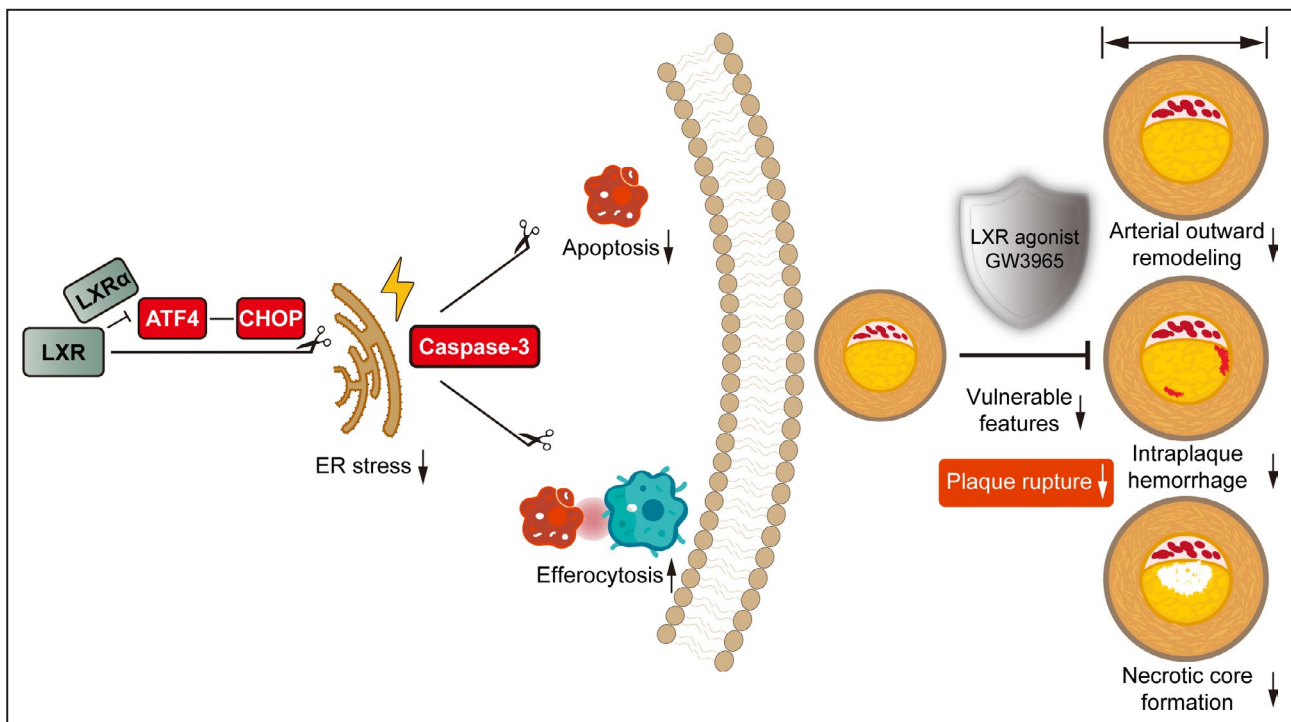


Figure 8. Protective functions of liver X receptor (LXR) α in established vulnerable plaques.

Activating LXR α alleviates apoptosis and enhances efferocytosis in macrophages. In mice, LXR α reduces arterial outward remodeling, intraplaque hemorrhage, and necrotic core formation, and eventually stabilizes vulnerable plaques. Endoplasmic reticulum (ER) stress-mediated C/EBP-homologous protein (CHOP) pathway is involved in these processes. ATF4 indicates activating transcription factor 4.

with simvastatin.³³ These pieces of evidence show that LXR may exert the atheroprotection apart from lipid-lowering effects. However, when it comes to vulnerable plaques, the underlying mechanisms are still little known.

Zooming into the biological processes that happened in the plaque, LXR agonists might exert focal protection in that lesional cell death was reduced while efferocytosis was enhanced. As we found LXR activation led to reduced plaque area, there might be other contributors involved. Apart from apoptosis and efferocytosis, monocyte recruitment and macrophage egress can also change lesion size. We then conducted complete blood counts and observed a decrease in the blood monocyte number/ratio after GW3965 intervention (Figure S11). Although the results according to published data indicate that LXR might normalize hypercholesterolemia-induced monocytosis in ApoE knockout mice,^{34,35} recent studies suggest that although monocyte recruitment to atherosclerotic lesions primarily contributes to macrophage accumulation in early lesion development, the local proliferation of lesional macrophages predominates in established atherosclerotic lesions.³⁶ Hence, whether decreases in blood monocytes alter macrophage accumulation in plaques and to what extent in our model merits further investigation. For

macrophage egress, monocyte-derived cells expressing C-C chemokine receptor type 7 (CCR7) (mainly macrophages and dendritic cells) can migrate out of the plaque in an LXR-dependent manner, reducing the cellularity in the plaque and thus the plaque size.³² Meanwhile, CCR7 is found to be upregulated during the phenotype shift to M1 macrophages.³⁷ We found cumulative CCR7⁺CD68⁺ cells in the subintimal and vessel wall area of vulnerable plaques, whereas scarce CCR7⁺ cells were presented in the GW3965 group (Figure S12). The CCR7⁺CD68⁺ cell population may be composed of detained monocyte-derived cells and proinflammatory M1 macrophages. Loss of CCR7⁺ cell detection is likely a consequence of cell egress or the resolution of inflammation after GW3965 treatment. As we did not see a notable difference in the ratio of lesional CD68⁺ cells between the 2 groups, we infer that CCR7-mediated cell egress may play an active role in protective effects of LXR in vulnerable plaques, but not a dominant one. We thus focused on lesional apoptosis/efferocytosis of macrophages and the participation of subcellular organelles in this circumstance. Reduced expression of basal caspase-12, found in the GW3965 group, was intriguing enough for us to explore the ER stress pathway. Mechanistically, LXR activation alleviated the expression of BiP, ATF4, and CHOP, 3 ER stress markers, and thus the lesional

stress (Figure 3). This finding is consistent with our previous work on myocardial ischemia/reperfusion injury,⁹ highlighting ER stress as a pivotal participant in cardiovascular diseases. In addition, it supports previous research into the vessel area, which links LXR and ER stress inhibition. In the hyperplastic neointima, LXR agonist T0901317 significantly decreases CD68⁺TUNEL⁺ double-positive macrophages and attenuates neointimal hyperplasia.³⁸ In another hypercholesterolemia mouse model, LXR α is able to increase the production of bioactive lipids and provide resistance to macrophage ER stress in atherosclerosis.³⁹ There are also studies exploring the protective role of CHOP gene knockout in atherosclerotic mice models.^{40–42} Referring to efferocytosis, previous reports have demonstrated that apoptotic cells activate LXR in phagocytes for their own clearance and lead to immune tolerance, and GW3965 treatment ameliorates lupus-like autoimmunity in mice.⁴³ In atherosclerosis, a combination of LXR/retinoic acid receptor α (RAR α) agonists may cooperate in the control of efficient phagocytosis.⁴⁴

LXR α and LXR β synergize to regulate genes that encode proteins involved in cholesterol uptake, efflux, transport, and excretion, named reverse cholesterol transport. Are both of these 2 isotypes equally essential to inhibit ER stress? Therefore, we conducted *in vitro* experiments to figure it out. We used 7-KC stimulation in cell experiments as a reflection of what happens in vulnerable plaques.⁴⁵ LXRs are activated by certain oxysterol ligands but not 7-KC. Meanwhile, nonsterol synthetic agonists (ie, GW3965 used in our study) have potent transcriptional activities; thus, they are useful tools for LXR research.²⁰ Unlike T0901317, GW3965 has no undesirable effects on farnesoid X receptors and androstane receptors. As 7-KC induced ER stress, LXR activation through GW3965 inhibited the UPR cascade (Figure S4). The dephosphorylation of 2 ER sensors, PERK and IRE1 α , as well as the downregulation of BiP, which binds to unfolded or misfolded proteins, might indicate the clearance of ER stress triggers, such as aberrant protein synthesis, lipid overloading, and oxidative stress.⁶ The peritoneal macrophage is a valuable tool for accessing specific protein functions *in vitro*. We preincubated LXR α knockout or LXR β knockout macrophages with LXR agonists before 7-KC stimulation in experiments. Activating LXR in the setting of LXR α genetic ablation blunted effects of GW3965 on ER stress inhibition, apoptosis alleviation, and efferocytosis enhancement, whereas the loss of LXR β had no apparent detrimental impact on LXR activation (Figures 4 and 5, Figures S7 and S8). A battery of genes is LXR-responsive, biological processes involved in cholesterol regulation, membrane phospholipid remodeling, innate immune response, phagocytosis, and so on. Considering the

powerful restoration of cell viability, we suppose that LXR activation motivates several antiapoptotic ways. The interaction network is worth detailed study in our future work.

To further explore if the plaque-stabilizing effect of LXR activation relies on intact LXR α function, general LXR α deletion was introduced in ApoE^{-/-} mice, and 2 comparisons were made: (1) After 4 weeks of plaque growth, LXR α ^{-/-}ApoE^{-/-} mice are more susceptible to lipid retention, with a concurrent trend of higher plasma cholesterol level and heavier plaque burden, compared with ApoE^{-/-} mice. This stage of vulnerable plaque seems relatively quiet, but with ongoing recruitment/proliferation of macrophages and the failed dissipation of lipid pool, molecular changes occur before cellular defects. (2) After 8 weeks of plaque progression, short-term events happen and are concomitant with evident phenotype anomalies, even though high-fat diets are retracted during the last 4 weeks. We infer that lipid toxicity may not be a determinant in the formation of advanced plaques. Effects of improved lipid profile attributable to GW3965 administration are partly preserved with solely activated LXR β , but plaques are still prone to rupture irrespective of LXR activation in LXR α ^{-/-}ApoE^{-/-} mice, and the macrophage dysfunction remained the same (apoptosis, impaired efferocytosis, and decompensated ER stress-related CHOP pathway). These findings highlight the importance of LXR α in treating vulnerable plaques (Figures 6 and 7). Taking the dumbness of LXR β and the adverse effects of LXR α into consideration, lesional drug delivery might be preferable to systemic activation of LXR α .

In summary, LXR α has a protective role in vulnerable plaques, and the details are described in Figure 8. Ligand activation of LXR reduces arterial outward remodeling, intraplaque hemorrhage, and necrotic core formation. These effects synergize to prevent plaque rupture. Mechanistically, activating LXR α alleviates apoptosis and enhances efferocytosis. And LXR α is able to correct the aberrant ER stress-mediated CHOP pathway in macrophages and vulnerable plaques. We suppose all these efforts will help to elucidate LXR biology and facilitate the eventual application of LXR therapies in cardiovascular diseases.

ARTICLE INFORMATION

Received July 10, 2020; accepted February 23, 2021.

Affiliations

Department of Cardiology, Renji Hospital, School of Medicine, Shanghai Jiao Tong University, Shanghai, China (X.C., Q.X., H.Z., N.G., Z.T., Q.S., J.P.); Cardiovascular Department of Shuguang Hospital, Affiliated to Shanghai University of Traditional Chinese Medicine, Shanghai, China (W.S.); and Department of Radiology, Renji Hospital, School of Medicine, Shanghai Jiao Tong University, Shanghai, China (B.S.).

Acknowledgments

We thank Dr Ancai Yuan, Dr Qingqi Ji, Dr Yanan Fu, and Dr Muting Feng (Shanghai Jiao Tong University, Shanghai, China) for providing us with liver X receptor (LXR) α -deficient and LXR β -deficient mice.

Sources of Funding

This work was supported by the National Natural Science Foundation of China (Nos. 81870338, 81570390, 81270374, and 81801650).

Disclosures

None.

Supplementary Material

Data S1

Table S1

Figures S1–S12

References 43,46–49

REFERENCES

- Arbab-Zadeh A, Fuster V. The myth of the "vulnerable plaque": transitioning from a focus on individual lesions to atherosclerotic disease burden for coronary artery disease risk assessment. *J Am Coll Cardiol*. 2015;65:846–855. DOI: 10.1016/j.jacc.2014.11.041.
- Pasterkamp G, den Ruijter HM, Libby P. Temporal shifts in clinical presentation and underlying mechanisms of atherosclerotic disease. *Nat Rev Cardiol*. 2017;14:21–29. DOI: 10.1038/nrcardio.2016.166.
- Bentzon JF, Otsuka F, Virmani R, Falk E. Mechanisms of plaque formation and rupture. *Circ Res*. 2014;114:1852–1866. DOI: 10.1161/CIRCRESAHA.114.302721.
- Kojima Y, Weissman IL, Leeper NJ. The role of efferocytosis in atherosclerosis. *Circulation*. 2017;135:476–489. DOI: 10.1161/CIRCULATIONAHA.116.025684.
- Feng BO, Yao PM, Li Y, Devlin CM, Zhang D, Harding HP, Sweeney M, Rong JX, Kuriakose G, Fisher EA, et al. The endoplasmic reticulum is the site of cholesterol-induced cytotoxicity in macrophages. *Nat Cell Biol*. 2003;5:781–792. DOI: 10.1038/ncb1035.
- Tabas I, Ron D. Integrating the mechanisms of apoptosis induced by endoplasmic reticulum stress. *Nat Cell Biol*. 2011;13:184–190. DOI: 10.1038/ncb0311-184.
- Levin N, Bischoff ED, Daige CL, Thomas D, Vu CT, Heyman RA, Tangirala RK, Schulman IG. Macrophage liver X receptor is required for antiatherogenic activity of LXR agonists. *Arterioscler Thromb Vasc Biol*. 2005;25:135–142. DOI: 10.1161/01.ATV.0000150044.84012.68.
- Joseph SB, McKilligin E, Pei L, Watson MA, Collins AR, Laffitte BA, Chen M, Noh G, Goodman J, Hagger GN, et al. Synthetic LXR ligand inhibits the development of atherosclerosis in mice. *Proc Natl Acad Sci USA*. 2002;99:7604–7609. DOI: 10.1073/pnas.112059299.
- He Q, Pu J, Yuan A, Lau WB, Gao E, Koch WJ, Ma XL, He B. Activation of liver-X-receptor alpha but not liver-X-receptor beta protects against myocardial ischemia/reperfusion injury. *Circ Heart Fail*. 2014;7:1032–1041. DOI: 10.1161/CIRCHEARTFAILURE.114.001260.
- Ji Q, Zhao Y, Yuan A, Pu J, He B. Deficiency of liver-X-receptor-alpha reduces glucose uptake and worsens post-myocardial infarction remodeling. *Biochem Biophys Res Commun*. 2017;488:489–495. DOI: 10.1016/j.bbrc.2017.05.072.
- Jin SX, Shen LH, Nie P, Yuan W, Hu LH, Li DD, Chen XJ, Zhang XK, He B. Endogenous renovascular hypertension combined with low shear stress induces plaque rupture in apolipoprotein E-deficient mice. *Arterioscler Thromb Vasc Biol*. 2012;32:2372–2379. DOI: 10.1161/ATVBAHA.111.236158.
- Peng S, Xu LW, Che XY, Xiao QQ, Pu J, Shao Q, He B. Atorvastatin inhibits inflammatory response, attenuates lipid deposition, and improves the stability of vulnerable atherosclerotic plaques by modulating autophagy. *Front Pharmacol*. 2018;9:438. DOI: 10.3389/fphar.2018.00438.
- Ding S, Lin N, Sheng X, Zhao Y, Su Y, Xu L, Tong R, Yan Y, Fu Y, He J, et al. Melatonin stabilizes rupture-prone vulnerable plaques via regulating macrophage polarization in a nuclear circadian receptor ROR α -dependent manner. *J Pineal Res*. 2019;67:e12581. DOI: 10.1111/jpi.12581.
- Xiao Q, Che X, Cai B, Tao Z, Zhang H, Shao Q, Pu J. Macrophage autophagy regulates mitochondria-mediated apoptosis and inhibits necrotic core formation in vulnerable plaques. *J Cell Mol Med*. 2020;24:260–275. DOI: 10.1111/jcmm.14715.
- Xu L, Su Y, Zhao Y, Sheng X, Tong R, Ying X, Gao L, Ji Q, Gao Y, Yan Y, et al. Melatonin differentially regulates pathological and physiological cardiac hypertrophy: crucial role of circadian nuclear receptor ROR α signaling. *J Pineal Res*. 2019;67:e12579. DOI: 10.1111/jpi.12579.
- Song J, Wang D, Chen H, Huang X, Zhong Y, Jiang N, Chen C, Xia M. Association of plasma 7-ketocholesterol with cardiovascular outcomes and total mortality in patients with coronary artery disease. *Circ Res*. 2017;120:1622–1631. DOI: 10.1161/CIRCRESAHA.117.31049.
- Shibata N, Glass CK. Macrophages, oxysterols and atherosclerosis. *Circ J*. 2010;74:2045–2051. DOI: 10.1253/circj.10-0860.
- Silvestre-Roig C, de Winther MP, Weber C, Daemen MJ, Lutgens E, Soehnlein O. Atherosclerotic plaque destabilization: mechanisms, models, and therapeutic strategies. *Circ Res*. 2014;114:214–226. DOI: 10.1161/CIRCRESAHA.114.302355.
- Hartwig H, Silvestre-Roig C, Hendrikse J, Beckers L, Paulin N, Van der Heiden K, Braster Q, Drechsler M, Daemen MJ, Lutgens E, et al. Atherosclerotic plaque destabilization in mice: a comparative study. *PLoS One*. 2015;10:e0141019. DOI: 10.1371/journal.pone.0141019.
- Hong C, Tontonoz P. Liver X receptors in lipid metabolism: opportunities for drug discovery. *Nat Rev Drug Discov*. 2014;13:433–444. DOI: 10.1038/nrd4280.
- Watanabe Y, Jiang S, Takabe W, Ohashi R, Tanaka T, Uchiyama Y, Katsumi K, Iwanari H, Noguchi N, Naito M, et al. Expression of the LXR α protein in human atherosclerotic lesions. *Arterioscler Thromb Vasc Biol*. 2005;25:622–627. DOI: 10.1161/01.ATV.0000154489.53077.4e.
- Terasaka N, Hiroshima A, Koieyama T, Ubukata N, Morikawa Y, Nakai D, Inaba T. T-901317, a synthetic liver X receptor ligand, inhibits development of atherosclerosis in LDL receptor-deficient mice. *FEBS Lett*. 2003;536:6–11. DOI: 10.1016/S0014-5793(02)03578-0.
- Verschuren L, de Vries-van der Weij J, Zadelaar S, Kleemann R, Kooistra T. LXR agonist suppresses atherosclerotic lesion growth and promotes lesion regression in apoE⁻³leiden mice: time course and mechanisms. *J Lipid Res*. 2009;50:301–311. DOI: 10.1194/jlr.M800374-JLR200.
- Naik SU, Wang X, Da Silva JS, Daje M, Macphhee CH, Reilly MP, Billheimer JT, Rothblat GH, Rader DJ. Pharmacological activation of liver x receptors promotes reverse cholesterol transport in vivo. *Circulation*. 2006;113:90–97. DOI: 10.1161/CIRCULATIONAHA.105.560177.
- Kirchgessner T, Sleph P, Ostrowski J, Lupisella J, Ryan C, Liu X, Fernando G, Grimm D, Shipkova P, Zhang R, et al. Beneficial and adverse effects of an LXR agonist on human lipid and lipoprotein metabolism and circulating neutrophils. *Cell Metab*. 2016;24:223–233. DOI: 10.1016/j.cmet.2016.07.016.
- Teupser D, Kretzschmar D, Tennert C, Burkhardt R, Wilfert W, Fengler D, Naumann R, Sippel AE, Thiery J. Effect of macrophage overexpression of murine liver X receptor-alpha (LXR-alpha) on atherosclerosis in LDL-receptor deficient mice. *Arterioscler Thromb Vasc Biol*. 2008;28:2009–2015. DOI: 10.1161/ATVBAHA.108.175257.
- Li G, Biju KC, Xu X, Zhou Q, Chen C, Valente AJ, He W, Reddick RL, Freeman GL, Ahuja SS, et al. Macrophage LXR α gene therapy ameliorates atherosclerosis as well as hypertriglyceridemia in LDLR(-/-) mice. *Gene Ther*. 2011;18:835–841. DOI: 10.1038/gt.2011.29.
- Tangirala RK, Bischoff ED, Joseph SB, Wagner BL, Walczak R, Laffitte BA, Daige CL, Thomas D, Heyman RA, Mangelsdorf DJ, et al. Identification of macrophage liver X receptors as inhibitors of atherosclerosis. *Proc Natl Acad Sci USA*. 2002;99:11896–11901. DOI: 10.1073/pnas.182199799.
- Bradley MN, Hong C, Chen M, Joseph SB, Wilpitz DC, Wang X, Lusis AJ, Collins A, Hseuh WA, Collins JL, et al. Ligand activation of LXR beta reverses atherosclerosis and cellular cholesterol overload in mice lacking LXR alpha and apoE. *J Clin Invest*. 2007;117:2337–2346. DOI: 10.1172/JCI31909.
- Bischoff ED, Daige CL, Petrowski M, Dedman H, Pattison J, Juliano J, Li AC, Schulman IG. Non-redundant roles for LXR α and LXR β in atherosclerosis susceptibility in low density lipoprotein receptor knock-out mice. *J Lipid Res*. 2010;51:900–906. DOI: 10.1194/jlr.M900096.
- Kappus MS, Murphy AJ, Abramowicz S, Ntonga V, Welch CL, Tall AR, Westerterp M. Activation of liver X receptor decreases atherosclerosis in Ldlr(-/-) mice in the absence of ATP-binding cassette transporters A1 and G1 in myeloid cells. *Arterioscler Thromb Vasc Biol*. 2014;34:279–284. DOI: 10.1161/ATVBAHA.113.302781.

32. Feig JE, Pineda-Torra I, Sanson M, Bradley MN, Vengrenyuk Y, Bogunovic D, Gautier EL, Rubinstein D, Hong C, Liu J, et al. LXR promotes the maximal egress of monocyte-derived cells from mouse aortic plaques during atherosclerosis regression. *J Clin Invest*. 2010;120:4415–4424. DOI: 10.1172/JCI38911.
33. Giannarelli C, Cimmino G, Connolly TM, Ibanez B, Ruiz JM, Alique M, Zafar MU, Fuster V, Feuerstein G, Badimon JJ. Synergistic effect of liver X receptor activation and simvastatin on plaque regression and stabilization: an magnetic resonance imaging study in a model of advanced atherosclerosis. *Eur Heart J*. 2012;33:264–273. DOI: 10.1093/eurheartj/ehr136.
34. Murphy AJ, Akhtari M, Tolani S, Pagler T, Bijl N, Kuo C-L, Wang MI, Sanson M, Abramowicz S, Welch C, et al. ApoE regulates hematopoietic stem cell proliferation, monocytosis, and monocyte accumulation in atherosclerotic lesions in mice. *J Clin Invest*. 2011;121:4138–4149. DOI: 10.1172/JCI57559.
35. Rasheed A, Tsai R, Cummins CL. Loss of the liver X receptors disrupts the balance of hematopoietic populations, with detrimental effects on endothelial progenitor cells. *J Am Heart Assoc*. 2018;7:e007787. DOI: 10.1161/JAHA.117.007787.
36. Robbins CS, Hilgendorf I, Weber GF, Theurl I, Iwamoto Y, Figueiredo J-L, Gorbato R, Sukhova GK, Gerhardt LMS, Smyth D, et al. Local proliferation dominates lesional macrophage accumulation in atherosclerosis. *Nat Med*. 2013;19:1166–1172. DOI: 10.1038/nm.3258.
37. Raggi F, Pelassa S, Pierobon D, Penco F, Gattorno M, Novelli F, Eva A, Varesio L, Giovarelli M, Bosco MC. Regulation of human macrophage M1–M2 polarization balance by hypoxia and the triggering receptor expressed on myeloid cells-1. *Front Immunol*. 2017;8:1097. DOI: 10.3389/fimmu.2017.01097.
38. Zhao Q, Zhou D, You H, Lou B, Zhang Y, Tian Y, Guo N, Chen X, Liu Y, Wu Y, et al. IFN- γ aggravates neointimal hyperplasia by inducing endoplasmic reticulum stress and apoptosis in macrophages by promoting ubiquitin-dependent liver X receptor- α degradation. *FASEB J*. 2017;31:5321–5331. DOI: 10.1096/fj.201700327R.
39. Erbay E, Babaev VR, Mayers JR, Makowski L, Charles KN, Snitow ME, Fazio S, Wiest MM, Watkins SM, Linton MF, et al. Reducing endoplasmic reticulum stress through a macrophage lipid chaperone alleviates atherosclerosis. *Nat Med*. 2009;15:1383–1391. DOI: 10.1038/nm.2067.
40. Thorp E, Li G, Seimon TA, Kuriakose G, Ron D, Tabas I. Reduced apoptosis and plaque necrosis in advanced atherosclerotic lesions of ApoE $^{-/-}$ and Ldlr $^{-/-}$ mice lacking CHOP. *Cell Metab*. 2009;9:474–481. DOI: 10.1016/j.cmet.2009.03.003.
41. Tsukano H, Gotoh T, Endo M, Miyata K, Tazume H, Kadomatsu T, Yano M, Iwawaki T, Kohno K, Araki K, et al. The endoplasmic reticulum stress-C/EBP homologous protein pathway-mediated apoptosis in macrophages contributes to the instability of atherosclerotic plaques. *Arterioscler Thromb Vasc Biol*. 2010;30:1925–1932. DOI: 10.1161/ATVBAHA.110.206094.
42. Gao J, Ishigaki Y, Yamada T, Kondo K, Yamaguchi S, Imai J, Uno K, Hasegawa Y, Sawada S, Ishihara H, et al. Involvement of endoplasmic stress protein C/EBP homologous protein in arteriosclerosis acceleration with augmented biological stress responses. *Circulation*. 2011;124:830–839. DOI: 10.1161/CIRCULATIONAHA.110.014050.
43. A-Gonzalez N, Bensinger SJ, Hong C, Beceiro S, Bradley MN, Zelcer N, Deniz J, Ramirez C, Díaz M, Gallardo G, et al. Apoptotic cells promote their own clearance and immune tolerance through activation of the nuclear receptor LXR. *Immunity*. 2009;31:245–258. DOI: 10.1016/j.immuni.2009.06.018.
44. Rebe C, Raveneau M, Chevriaux A, Lakomy D, Sberna AL, Costa A, Bessede G, Athias A, Steinmetz E, Lobaccaro JM, et al. Induction of transglutaminase 2 by a liver X receptor/retinoic acid receptor alpha pathway increases the clearance of apoptotic cells by human macrophages. *Circ Res*. 2009;105:393–401. DOI: 10.1161/CIRCRESAHA.109.201855.
45. Dickhout JG, Colgan SM, Lhotak S, Austin RC. Increased endoplasmic reticulum stress in atherosclerotic plaques associated with acute coronary syndrome: a balancing act between plaque stability and rupture. *Circulation*. 2007;116:1214–1216. DOI: 10.1161/CIRCULATIONAHA.107.728378.
46. Schrijvers DM, De Meyer GR, Kockx MM, Herman AG, Martinet W. Phagocytosis of apoptotic cells by macrophages is impaired in atherosclerosis. *Arterioscler Thromb Vasc Biol*. 2005;25:1256–1261. DOI: 10.1161/01.ATV.0000166517.18801.a7.
47. Kojima Y, Volkmer J-P, McKenna K, Civelek M, Lusis AJ, Miller CL, Direnzo D, Nanda V, Ye J, Connolly AJ, et al. CD47-blocking antibodies restore phagocytosis and prevent atherosclerosis. *Nature*. 2016;536:86–90. DOI: 10.1038/nature18935.
48. Seneviratne AN, Edsfieldt A, Cole JE, Kassiteridi C, Swart M, Park I, Green P, Khoiratty T, Saiba D, Goddard ME, et al. Interferon regulatory factor 5 controls necrotic core formation in atherosclerotic lesions by impairing efferocytosis. *Circulation*. 2017;136:1140–1154. DOI: 10.1161/CIRCULATIONAHA.117.027844.
49. Proto JD, Doran AC, Gusarova G, Yurdagul A Jr, Sozen E, Subramanian M, Islam MN, Rymond CC, Du J, Hook J, et al. Regulatory T cells promote macrophage efferocytosis during inflammation resolution. *Immunity*. 2018;49:666–677.e666. DOI: 10.1016/j.immuni.2018.07.015.

SUPPLEMENTAL MATERIAL

Data S1. Supplemental Methods

Supplemental animal experiment

ApoE^{-/-} mice were housed under specific pathogen-free conditions and allowed free access to water in a 12-hour light/dark cycle, with room temperature at 21± 2°C.

Magnetic resonance imaging (MRI) scans

The parameters were listed below: image size, 256*256; field of view: 25 mm*25 mm; slice thickness, 0.5 mm; slice, 20; echo time, 5 ms; repetition time, 950 ms; resolution, 0.098 mm*0.098 mm. The images were anonymized and analyzed in DICOM Library online.

Tissue collection

A hanging perfusion system at a flow rate of 2 ml/min was applied for 15 minutes, with pre-cooled saline placed at 1-meter high and cannula inserted into the left ventricle (outflow via a cut in the right atrium). Connected and fat tissues were removed around the common carotid artery under a microscope, then a gross picture was taken by a camera. The left common carotid artery was harvested and frozen in optimal cutting temperature (OCT) embedding compound (Sakura, Netherlands), then stored at -80°C.

Histological staining of Murine Left Common Carotid Artery

6-µm cryosections of left common carotid arteries were taken using Cryotome® FE & FSE (Thermo Scientific, USA). Serial sections of a 250-µm interval were processed with hematoxylin and eosin, Oil Red O, and Masson's trichrome staining. Images were captured under the identical microscope, camera, and light conditions. Lesion area quantification was performed by drawing around the atherosclerotic lesions and the

artery wall using ImageJ software (Version 1.8.0, USA) as previously described. The segmental lesion areas were averaged to obtain the mean lesion area. Lesion volume was estimated via area under the curve. In hematoxylin and eosin staining, intraplaque hemorrhage components such as erythrocytes and fibrin clots were stained bright red and distinct pink, which is distinguishable from the pink of other cells or tissues. Necrotic areas were defined as acellular non-fibrotic regions, only areas larger than 1000 μm^2 were included. Lipid deposition and collagen content were detected by Oil Red O and Masson's trichrome staining respectively, measurements were performed using ImageJ software.

Immunofluorescence

Section levels with lesion areas ranked among the top three were chosen to undergo further immunofluorescence processes to acquire the averages of indicated parameters. Frozen sections of left common carotid arteries were fixed in 10% neutral buffered formalin for 20 minutes followed by PBS washing, then permeabilized with cold methanol for 15 minutes. After washing with PBS, slides were incubated in blocking buffer containing 5% BSA, stained with the specific primary antibody (CD68, 1:200; α -SMA, 1:100; LXR α , 1:100; LXR β , 1:40; Cleaved Caspase-3, 1:200; Caspase-9, 1:200; Caspase-12, 1:200; BiP, 1:200; ATF4, 1:200; CHOP, 1:200; CCR7, 1:200) overnight, and then stained with the corresponding secondary antibody. VECTASHIELD® antifade mounting medium with DAPI (Vector Laboratories, USA) was used to identify nuclei and mounting. Vessels were imaged using a fluorescence microscope (Leica DM3000B, Germany). The positive staining area (% of lesion area)

was quantified using ImageJ software (Version 1.8.0, USA) as previously described.

In situ lesional apoptosis and efferocytosis assay

A similar strategy was applied to section selection as in the immunofluorescence experiments. Slides containing frozen sections were fixed in 10% neutral buffered formalin for 20 minutes. After washing with PBS, slides were permeabilized with cold 0.3% Triton-100 for 10 minutes followed by another PBS washing. Sections were incubated with TUNEL staining reagents at room temperature for 60 minutes and then washed three times with PBS. Sections were then blocked with 5%BSA for 60 minutes, incubated overnight at 4°C with an anti-CD68 antibody (1:200). At last, slides were incubated with fluorescently-labeled secondary antibodies and counterstained with DAPI. In situ efferocytosis was quantified by counting TUNEL-positive nuclei that were associated with macrophages ('associated'), indicative of efferocytosis, or not associated with macrophages ('free')⁴⁶⁻⁴⁸. TUNEL-positive nuclei surrounded by or in contact with neighboring CD68+ macrophages indicated macrophage-associated apoptotic cells. Free apoptotic cells exhibited nuclear condensation and were not in contact with neighboring macrophages.

In vivo efferocytosis assay

This assay was performed as previously described^{43, 49}. Apoptotic cells (ACs) were generated by irradiating Jurkat cells under a UV (254 nm) lamp in PBS for 15 minutes followed by incubation under normal cell culture conditions for 3 hours. This method routinely yielded greater than 75% Annexin V-positive cells. ACs were incubated with CellTrace™ CFSE reagent (Invitrogen, USA) for 20 minutes at 37°C. Before tissue

collection, mice from GW3965 or Vehicle group were injected intraperitoneally with 5×10^6 CFSE-labeled apoptotic cells in 500 μ L PBS. After 1 hour of incubation, blood was withdrawn followed by peritoneal lavage (10 ml of cold PBS three times). After RBC lysis, the peritoneal cells were resuspended in PBS and stained for macrophage marker (F4/80, 1:100, 30min at room temperature) for subsequent flow cytometry analysis. Samples were processed on the FACSCelesta platform (BD, USA) and analyzed with the FlowJo software (Version 10.4, USA). Cell populations were first gated for non-lymphocytes (forward scatter versus side scatter), then gated for F4/80 positive cells (fluorescence intensity of PE). After excluding doublets (forward scatter versus forward scatter width), macrophages were further gated for CFSE positive cells. Efferocytosis was quantified as the percentage of F4/80 positive macrophages that had taken up one or more CFSE-labeled apoptotic cells.

Real-time quantitative PCR

RNA was extracted from samples using the Trizol (Ambion, USA) reagent. The purity of RNA was assessed by absorbance at 260 and 280 nm using the NanoDrop spectrophotometer (Thermo Scientific, USA). cDNA was synthesized using PrimeScript RT Master Mix kit (Takara, Japan). Quantitative RT-PCR was performed using a LightCycler® 480 System (Roche, Germany) and SYBR Premix Ex Taq kit (Takara, Japan). All samples were analyzed in triplicate and were normalized to Gapdh or Actb, depending on the immunoblot inner control choice under the same treatment. The $2^{-\Delta\Delta C_t}$ method was used to analyze the relative changes in gene expression.

Western blotting assay

Cells were lysed in complete lysis-M (Roche, Germany) plus the protease and phosphatase inhibitor (Thermo Scientific, USA) containing 1% β -Mercaptoethanol and heated at 100°C for 10 minutes. Lysates were separated on 10% SDS-PAGE gels at 70V, then 120V for 1.5 hours, and electro-transferred to 0.45-mm PVDF membranes (Millipore, USA) at 250mA for 80-100 minutes. Membranes were incubated in TBST (TBS with 0.1% Tween 20) containing 5% non-fat milk at room temperature, then overnight at 4°C with primary antibodies in blocking buffer (LI-COR, USA), and detected using HRP-conjugated secondary antibodies (Jackson ImmunoResearch, USA). Densitometry was performed using Gel-Pro Analyzer software (Version 4.0, USA).

Macrophage apoptosis experiment

The apoptosis experiment was carried out in immunoblot assay and TUNEL staining (In Situ Cell Death Detection Kit Fluorescein, Roche, Germany). In brief, macrophages under different treatments were rinsed with PBS and fixed in 4% paraformaldehyde for 1 hour at room temperature, then washed with PBS, and permeabilized with freshly prepared 0.1% Triton X-100 in PBS for 10 minutes on ice. After washing with PBS, the coverslips were overlaid with 20 μ l of TUNEL reaction mixture and incubated for 60 minutes at room temperature. Finally, cells were washed in PBS, and coverslips were mounted onto slides after staining with DAPI. Cells were imaged as mentioned above. The percentage of TUNEL-positive nuclei (green) was quantified using ImageJ software.

In vitro efferocytosis assay

Apoptotic Jurkat cells (Acs) were incubated with CellTrace™ Violet or CFSE reagent (Invitrogen, USA) for 20 minutes at 37°C. Fluorescent ACs were added to macrophages for 45 minutes with the 5:1 ratio, followed by vigorous washing three times with PBS. Cells were either imaged using an inverted fluorescence microscope (Leica DM2500, Germany) or dissociated from the wells and analyzed by flow cytometry (Beckman CytoFLEX, USA). We used histograms to display macrophages with or without Acs (relative fluorescence intensity) on the x-axis and the number of events (cell count) on the y-axis.

Supplemental statistical analysis

In our pilot study, we examined the effects of GW3965 on individual lesion growth using MRI scans. The preliminary data show that difference in the mean and difference in the standard deviation are 1.2 and 0.5 after 4 weeks of drug administration. Sample size calculations were performed with PS: Power and Sample Size Calculation (Version 3.1.6, USA). To achieve power (1- β) of 0.8 and α of 0.05 to detect this difference would require 4 animals. According to our randomization and blinding strategy, mice were weighed and ranked in ascending order, then allocated to different groups in order i.e. mouse 1 group 1, mouse 2 group 2, mouse 3 group 3, mouse 4 group 1, etc. Group allocation was coded by Dr. Song, and the surgery was operated by Dr. Che. Dr. Zhang did the drug injection part. The pilot study and MRI scans were carried out by Dr. Xiao, assisted by Dr. Sun.

Supplemental Table

Table S1. Key resources table.

Reagent or Resource	Source	Identifier
Antibodies		
Rat anti-CD68	Abcam	Cat# ab53444; RRID: AB_869007
Rabbit anti- α -SMA	Abcam	Cat# ab5694; RRID: AB_2223021
Rabbit anti-LXR α	Abcam	Cat# ab3585; RRID: AB_303930
Rabbit anti-LXR β	Santa Cruz Biotechnology	Cat# sc-1001; RRID: AB_632063
Rabbit anti-Cleaved Caspase-3 (Asp175)	Cell Signaling Technology	Cat# 9664T; RRID: AB_2070042
Rabbit anti-Caspase-9	Abcam	Cat# ab202068; N/A
Rabbit anti-Caspase-12	Cell Signaling Technology	Cat# 2202S; RRID: AB_2069200
Rabbit anti-BiP	Cell Signaling Technology	Cat# 3177T; RRID: AB_2119845
Rabbit anti-ATF-4	Cell Signaling Technology	Cat# 11815S; RRID: AB_2616025
Mouse anti-CHOP	Cell Signaling Technology	Cat# 2895T; RRID: AB_2089254
PE Rat Anti-Mouse F4/80	BD Biosciences	Cat# 565410; RRID: AB_2687527
Rabbit anti-CCR7	Abcam	Cat# 2 ab32527; RRID: AB_726208
Donkey anti-rat (AF594)	Thermo Fisher Scientific	Cat# A-21209; RRID: AB_2535795
Donkey anti-rabbit (AF488)	Thermo Fisher Scientific	Cat# A-21206; RRID: AB_2535792
Goat anti-rabbit (AF594)	Thermo Fisher Scientific	Cat #A-11012; RRID: AB_141359
Goat anti-mouse (AF555)	Thermo Fisher Scientific	Cat# A-21422; RRID: AB_141822
Goat anti-rat (AF488)	Thermo Fisher Scientific	Cat# A-11006; RRID: AB_141822
Rabbit anti-GAPDH	Cell Signaling Technology	Cat# 5174T; RRID: AB_10622025
Rabbit anti- β -Actin	Cell Signaling Technology	Cat# 4970T; RRID: AB_2223172
Rabbit anti-IRE1 α	Cell Signaling Technology	Cat# 3294T; RRID: AB_823545

Rabbit anti-p-IRE1 α (Ser724)	Novus Biologicals	Cat# NB100-2323SS; RRID: AB_10145203
Rabbit anti-PERK	Cell Signaling Technology	Cat# 5683T; RRID: AB_10831515
Rabbit anti-p-PERK (Thr980)	Cell Signaling Technology	Cat# 3179S; RRID: AB_2095853
Mouse anti-LXR α	Abcam	Cat# ab41902; RRID: AB_776094
Goat anti-rabbit (HRP)	Jackson ImmunoResearch	Cat# 111-035-003; RRID: AB_2313567
Goat anti-mouse (HRP)	Jackson ImmunoResearch	Cat# 115-035-003; RRID: AB_10015289

Oligonucleotides (Mouse)

Gapdh Forward AGGTCGGTGTGAACGGATTTG	PrimerBank	https://pga.mgh.harvard.edu/primerbank/
Gapdh Reverse TG TAGACCATGTAGTTGAGGTCA	PrimerBank	-
Chop Forward CTGGAAGCCTGGTATGAGGAT	PrimerBank	-
Chop Reverse CAGGGTCAAGAGTAGTGAAGGT	PrimerBank	-
Atf4 Forward CCTGAACAGCGAAGTGTGG	PrimerBank	-
Atf4 Reverse TGGAGAACCCATGAGGTTTCAA	PrimerBank	-
sXBP1 Forward CTGAGTCCGCAGCAGGTG	PrimerBank	-
sXBP1 Reverse GACCTCTGGGAGTTCCTCCA	PrimerBank	-
Abca1 Forward AAAACCGCAGACATCCTTCAG	PrimerBank	-
Abca1 Reverse CATACCGAAACTCGTTCACCC	PrimerBank	-
Abcg1 Forward CTTTCCTACTCTGTACCCGAGG	PrimerBank	-
Abcg1 Reverse CGGGGCATTCCATTGATAAGG	PrimerBank	-
Actb Forward GGCTGTATTCCCCTCCATCG	PrimerBank	-
Actb Reverse CCAGTTGGTAACAATGCCATGT	PrimerBank	-

Other reagents and materials

DMEM	Gibco	Cat# 10569-010
------	-------	----------------

FBS	Gibco	Cat# 10099-141
7-KC	Sigma-Aldrich	Cat# C2394
GW3965	MedChemExpress	Cat# HY-10627A
Brewer's thioglycollate medium	Sigma-Aldrich	Cat# 70157
Trizol	Ambion	Cat# 15596026
PrimeScript RT Master Mix kit	Takara	Cat# RR036A
Complete lysis-M	Roche	Cat# 04719964001
Protease and phosphatase inhibitor	Thermo Scientific	Cat# 78443
0.45-mm PVDF membrane	Millipore	Cat# IPVH00010
Odyssey® blocking buffer (PBS)	LI-COR	Cat# 927-40000
In Situ Cell Death Detection Kit Fluorescein	Roche	Cat# 11684795910
VECTASHIELD® antifade mounting medium with DAPI	Vector Laboratories	Cat# H-1200
CellTrace™ Violet reagent	Invitrogen	Cat# C34571
CellTrace™ CFSE reagent	Invitrogen	Cat# C34570
ApoE ^{-/-} mice on a C57BL/6 background	GemPharmatech	Cat# T001458
High-fat diet	Research Diets	Cat# D12109
OCT embedding compound	Sakura	Cat# 4583
Pentobarbital sodium	Tocris Bioscience	Cat# 4579
Lidocaine	Hualu	Cat# 1005741
Isoflurane	RWD	Cat# R510-22
Gas anesthesia machine	RWD	Cat# R500

Supplemental Figures

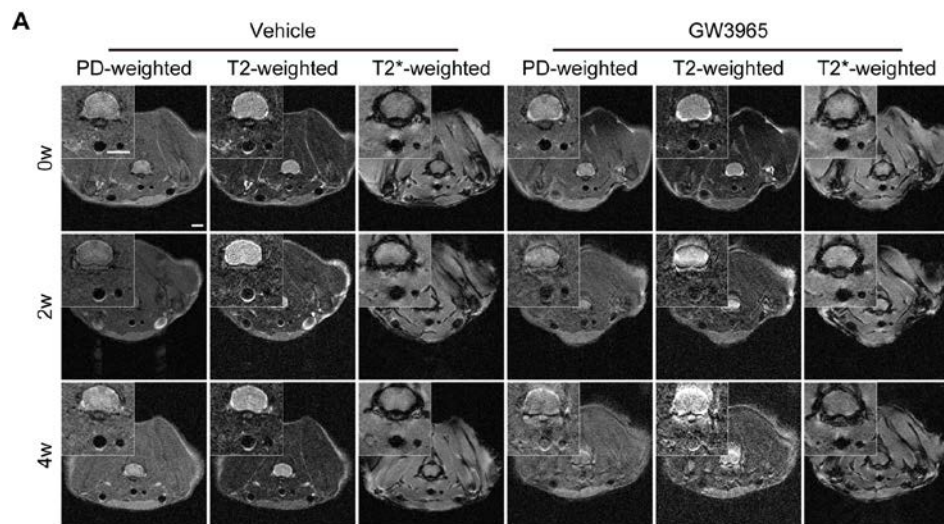


Figure S1. Representative images from 3 MRI sequences.

3 MRI sequences (PD, T2, T2 star) were applied. **A**, Representative MRI images show plaque changes at 0w, 2w, and 4w from the Vehicle and GW3965 groups. Scale bar= 1000 μm .

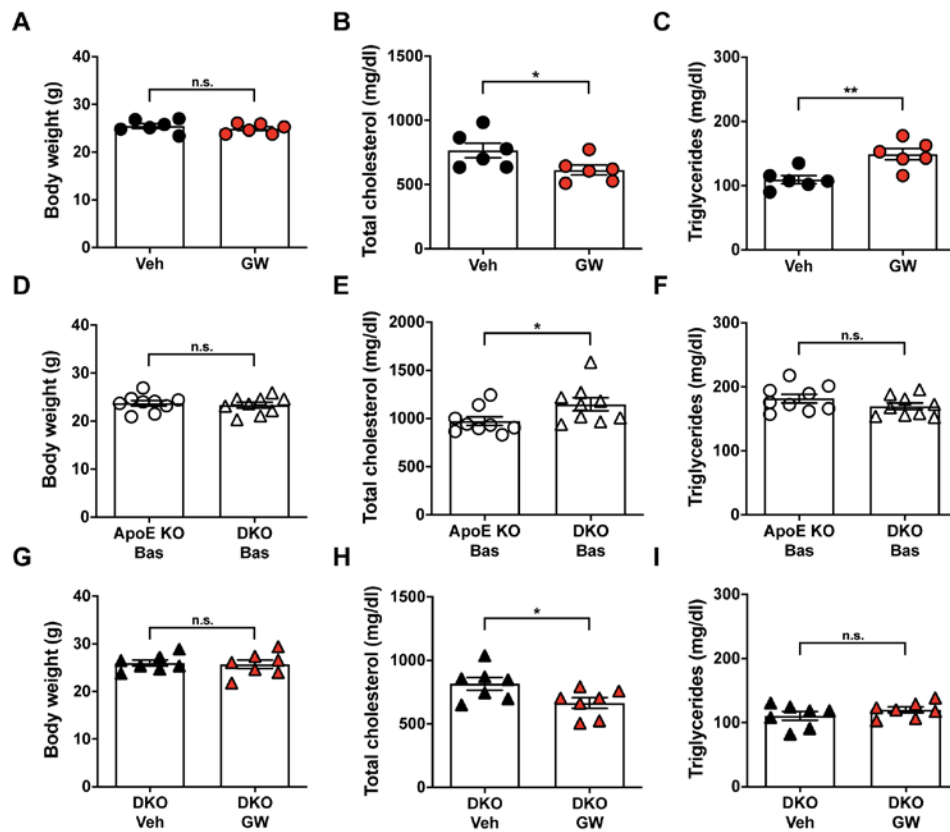


Figure S2. Quantification of the body weight and plasma lipid levels.

Quantification of the body weight and plasma lipid levels of different groups. **A, D, and G,** Graph shows the body weight measurements. **B, E, and H,** Graph shows the total cholesterol measurements. **C, F, and I,** Graph shows the triglycerides measurements. n=6 in both ApoE^{-/-} Vehicle and ApoE^{-/-} GW3965 groups; n=9 in both ApoE^{-/-} Baseline and LXRα^{-/-}ApoE^{-/-} Baseline groups; n=7 in both LXRα^{-/-}ApoE^{-/-} Vehicle and LXRα^{-/-} ApoE^{-/-} GW3965 groups. Data are presented as mean± SEM and ‘n’ refers to the number of mice. n.s. is short for not significant, *p< 0.05, **p< 0.01 [ApoE^{-/-} Vehicle versus ApoE^{-/-} GW3965: two-tailed unpaired Student’s *t* test for (A-C); ApoE^{-/-} Baseline versus LXRα^{-/-}ApoE^{-/-} Baseline: two-tailed unpaired Student’s *t* test for (D-F); LXRα^{-/-} ApoE^{-/-} Vehicle versus LXRα^{-/-} ApoE^{-/-} GW3965: two-tailed unpaired Student’s *t* test for (G-I)].

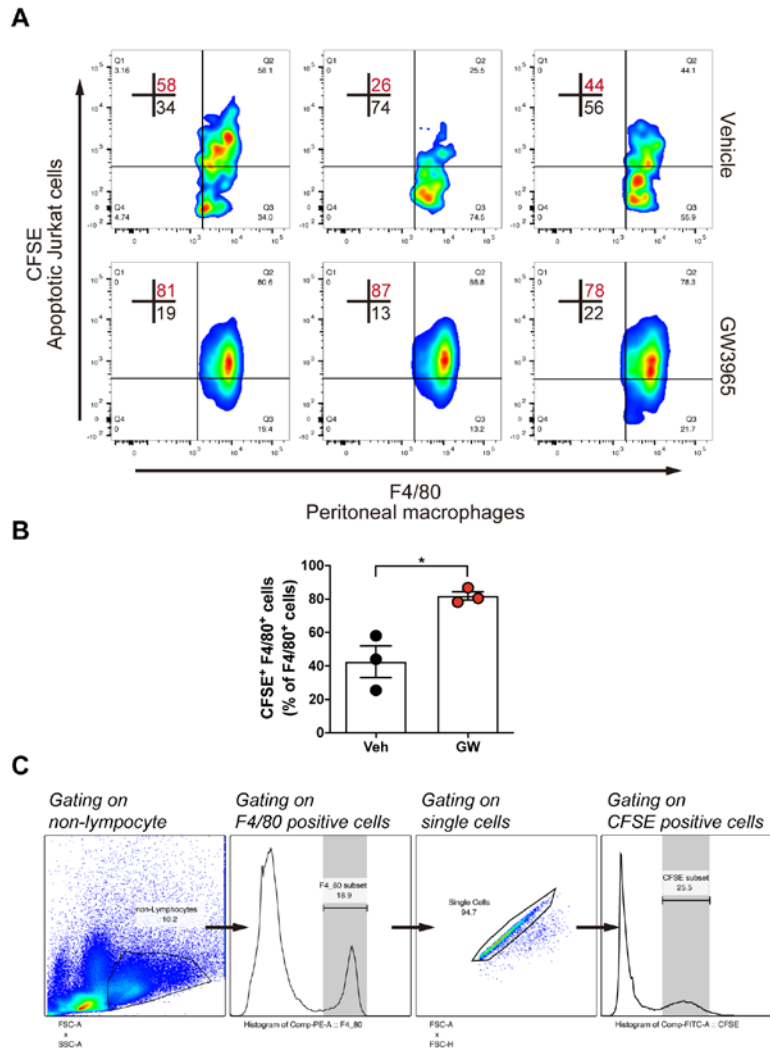


Figure S3. LXR activation enhances peritoneal uptake of labeled apoptotic cells.

The percentage of CFSE-labeled apoptotic jurkat cells associated with F4/80 positive macrophages was determined by flow cytometry (n=3). **A**, Results from three separate mice are shown for each treatment. **B**, Graph shows the quantification of CFSE⁺F4/80⁺ cells (% of F4/80⁺ cells, n=3) in **(A)**. **C**, The gating strategy of the flow cytometry assay. Data are presented as mean± SEM and ‘n’ refers to the number of mice. *p< 0.05 [two-tailed unpaired Student’s *t* test for (B)].

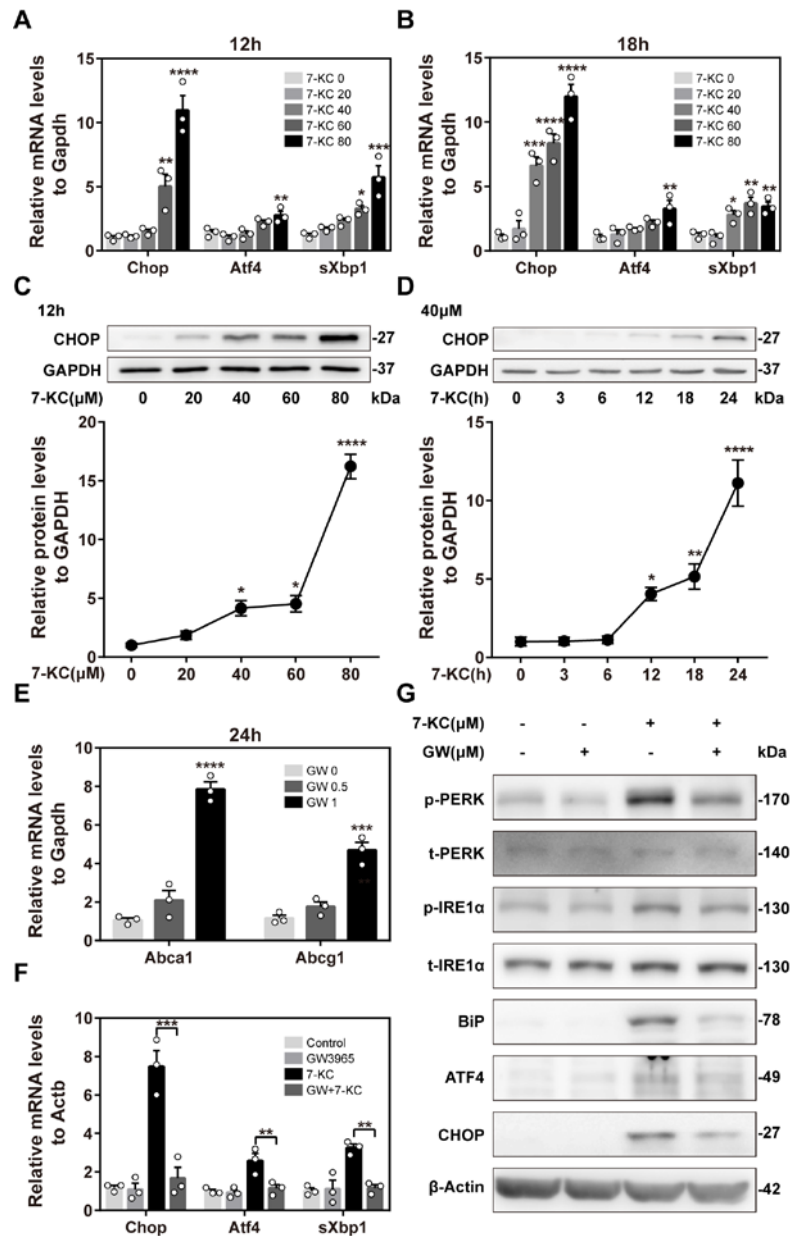


Figure S4. Activation of LXR inhibits 7-KC-induced ER stress in macrophages.

Activating LXR inhibits 7-KC-induced ER stress in cell experiments. **A**, and **B**, Raw 264.7 cells were treated with the indicated concentrations (0, 20, 40, 60, 80 µM) of 7-KC, RNA was extracted at 12 and 18 hours. Gene expressions of ER stress markers (Chop, Atf4, and sXbp1) were assessed by qPCR (n=3). Graphs show the relative mRNA levels to Gapdh. **C**, and **D**, With the concentration gradient above, proteins were collected at 12 hours. Using a specific dose of 7-KC (40 µM), another set of

treatments was conducted at different time points (0, 3, 6, 12, 18, 24 hours). Protein expression of CHOP in Raw 264.7 cells was detected by western blotting (n=3). Graphs show the relative protein expression to GAPDH. CHOP expression began to increase significantly during 12 hours of 7-KC treatment with 40 μ M. **E**, Cells were incubated with increasing concentrations of GW3965 for 24 hours, then RNA was extracted, and qPCR (n=3) was taken. Gene expressions of Abca1 and Abcg1 increased significantly at 1 μ M upon GW3965 treatment. **F**, Raw 264.7 cells were pretreated with or without GW3965 (1 μ M) for 24 hours, then incubated with or without 7-KC (40 μ M) for an additional 24 hours, RNA was extracted and proteins were collected. Gene expressions of ER stress markers were assessed by qPCR (n=3). Graphs show the relative mRNA levels to Gapdh. **G**, Protein expressions were detected by western blotting (n=3). The protein-specific antibodies are indicated. Activation of LXR has a broad inhibitory effect on the UPR pathways. The phosphorylation of PERK and IRE1 α , as initial indicators of UPR, were compared with their total forms. Data are presented as mean \pm SEM and 'n' refers to the number of independent experiments taken. *p< 0.05, **p< 0.01, ***p< 0.001, ****p< 0.0001 compared with control or indicated groups [one-way ANOVA followed by Dunnett's multiple comparisons test for (A-E); one-way ANOVA followed by Tukey's multiple comparisons test for (F)].

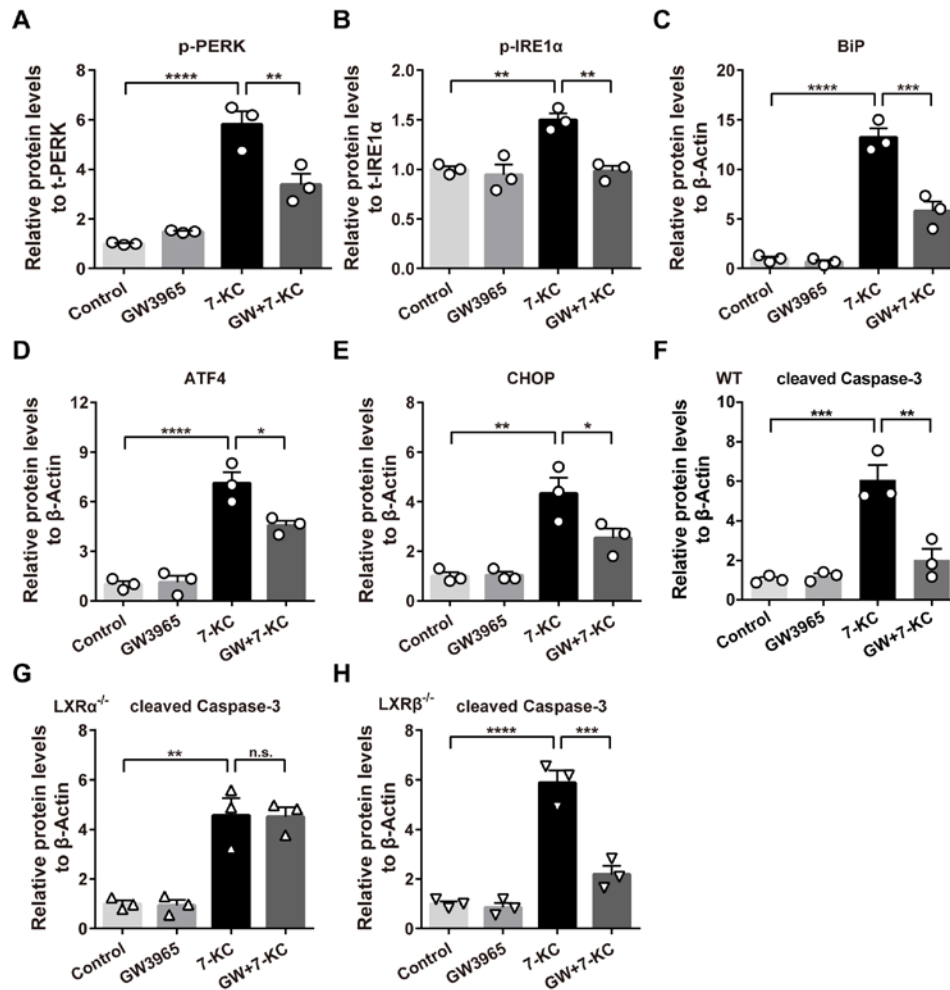


Figure S5. Quantification of western blotting assay.

ER stress markers and cleaved Caspase-3 protein expressions in different groups were evaluated via the western blotting assay. **A**, Graph shows the relative p-PERK protein levels to t-PERK. **B**, Graph shows the relative p-IRE1 α protein levels to t-IRE1 α . **C**, Graph shows the relative BiP protein levels to β -Actin. **D**, Graph shows the relative ATF4 protein levels to β -Actin. **E**, Graph shows the relative CHOP protein levels to β -Actin. **F**, Graph shows the relative cleaved Caspase-3 protein levels to β -Actin in WT macrophages. **G**, Graph shows the relative cleaved Caspase-3 protein levels to β -Actin in LXR α -deficient macrophages. **H**, Graph shows the relative cleaved Caspase-3 protein levels to β -Actin in LXR β -deficient macrophages. Data are presented as

mean \pm SEM and the number of independent experiments taken was 3. n.s. is short for not significant, * $p < 0.05$, ** $p < 0.01$, *** $p < 0.001$, **** $p < 0.0001$ [one-way ANOVA followed by Tukey's multiple comparisons test for (A-H)].

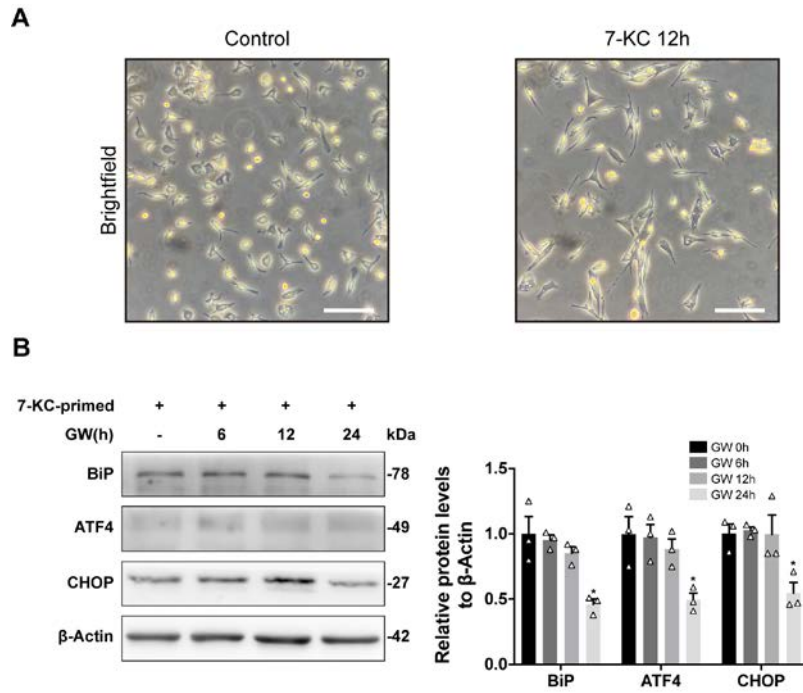


Figure S6. Effects of LXR activation on 7-KC primed macrophages.

Peritoneal macrophages were primed with 7-KC for 12 hours. Then, GW3965 was introduced to the primed macrophages for a duration of 0h, 6h, 12h, 24h. **A**, Representative images of morphology changes after 7-KC stimulation. Scale bar= 50 μ m. **B**, Western blotting of CHOP, ATF4, and BiP protein expression (n=3). Data are presented as mean \pm SEM and 'n' refers to the number of independent experiments taken. *p< 0.05 compared with control groups [one-way ANOVA followed by Dunnett's multiple comparisons test for (B)].

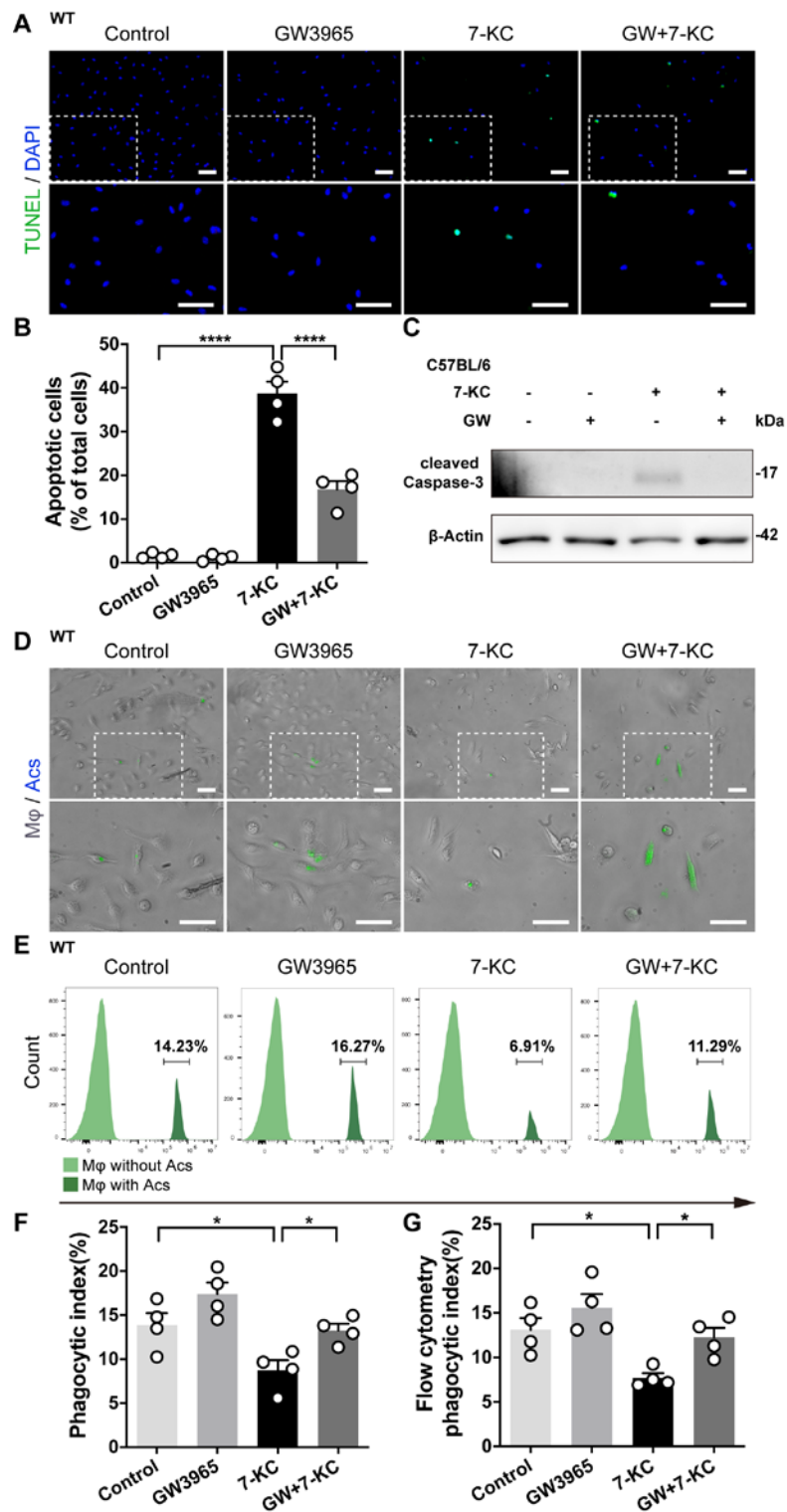


Figure S7. LXR agonists alleviated apoptosis and impaired efferocytosis induced by 7-KC in WT macrophages.

GW3965 was added to 7-KC-flamed peritoneal macrophages from C57BL/6 mice. **A** and **B**, Representative photomicrographs show that activating LXR in WT

macrophages reduced the TUNEL-positive areas (green) induced by 7-KC. Dotted squares (first row in **A**) indicate the corresponding part of enlarged pictures (second row in **A**). Scale bar= 100 μ m. The graph shows apoptotic cell measurements (n=4).

C, Western blotting of cleaved Caspase-3 protein expression (n=3) was also adopted to access the protective effects of LXR activation on apoptosis. **D** and **E**, In vitro efferocytosis assay (n=4) was conducted using peritoneal macrophages from WT mice. Dotted squares (first row in **D**) indicate the corresponding part of the enlarged pictures (second row in **D**). Scale bar= 100 μ m. Representative photomicrographs show that more free macrophages were observed upon 7-KC stimulation, while LXR activation reversed this defective efferocytosis. Flow cytometry analysis (n=4) was adopted as well. **F** and **G**, Graphs show the phagocytic index measurements. Activating LXR enhanced efferocytosis that was impaired by 7-KC in WT macrophages. The phagocytic index is defined as the ratio of apoptotic cells-associated macrophages to total cells. Data are presented as mean \pm SEM and 'n' refers to the number of independent experiments taken. *p< 0.05, ****p< 0.0001 [one-way ANOVA followed by Tukey's multiple comparisons test for (B), (F), and (G)].

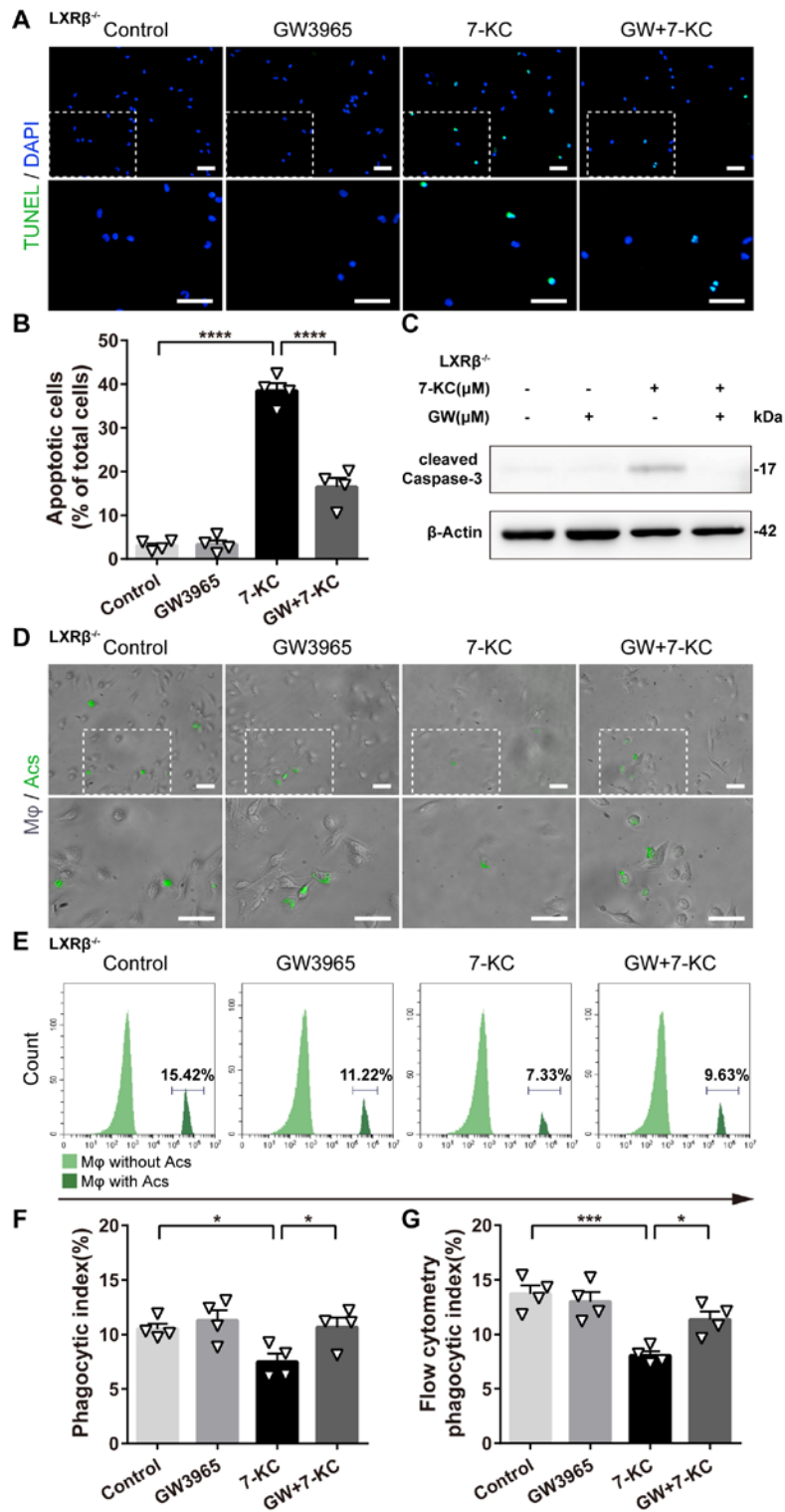


Figure S8. LXR agonists reserve properties on apoptosis alleviation and efferocytosis enhancement in the setting of genetic ablation of $LXR\beta$.

GW3965 was added to 7-KC-flamed peritoneal macrophages from $LXR\beta^{-/-}$ mice. **A** and **B**, Representative photomicrographs show that activating LXR in $LXR\beta$ -deficient

macrophages reduced the TUNEL-positive areas (green) induced by 7-KC. Dotted squares (first row in **A**) indicate the corresponding part of enlarged pictures (second row in **A**). Scale bar= 100 μ m. The graph shows apoptotic cell measurements (n=4). **C**, Western blotting of cleaved Caspase-3 protein expression (n=3) was also adopted to access the protective effects of LXR activation on apoptosis. **D** and **E**, In vitro efferocytosis assay (n=4) was conducted using peritoneal macrophages from LXR β knockout mice. Dotted squares (first row in **D**) indicate the corresponding part of the enlarged pictures (second row in **D**). Scale bar= 100 μ m. Representative photomicrographs show that more free macrophages were observed upon 7-KC stimulation, while LXR activation in LXR β -deficient settings reversed this defective efferocytosis. Flow cytometry analysis (n=4) was adopted as well. **F** and **G**, Graphs show the phagocytic index measurements. Activating LXR enhanced efferocytosis that was impaired by 7-KC in LXR β -deficient macrophages. The phagocytic index is defined as the ratio of apoptotic cells-associated macrophages to total cells. Data are presented as mean \pm SEM and 'n' refers to the number of independent experiments taken. *p< 0.05, ***p< 0.001, ****p< 0.0001 [one-way ANOVA followed by Tukey's multiple comparisons test for (B), (F), and (G)].

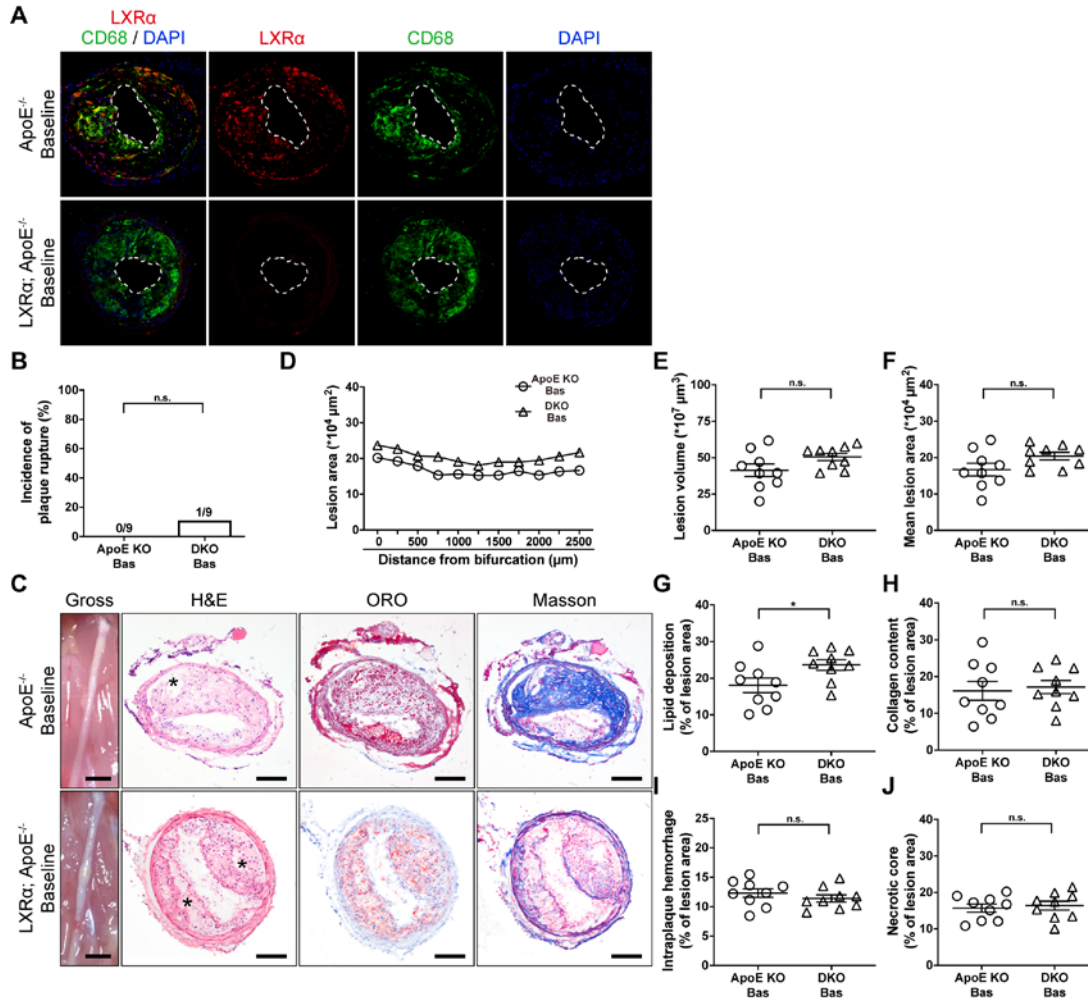


Figure S9. Characteristics of plaque vulnerability in ApoE^{-/-} and LXRα^{-/-}ApoE^{-/-} mice at 4 weeks.

Vulnerable plaques were established in LXRα-sufficient and LXRα-deficient mice. Plaques at 4 weeks were set as the baseline. **A**, Validation of general LXRα knockout used immunofluorescence staining. Representative photomicrographs of carotid sections stained with antibodies against LXRα (red) and CD68 (green), and counterstained with DAPI (blue). Dotted lines denote the lumen area. Scale bar= 100 μm . **B**, Graph shows the measurements of the incidence of plaque rupture (%), n=9). **C**, Representative gross pictures and photomicrographs of carotid frozen sections stained with hematoxylin and eosin, oil red O, and Masson's trichrome staining.

Asterisks represent the necrotic core areas. Scale bar= 1000 (first column in **C**) and 100 μm . **D**, **E**, and **F**, Graphs show the measurements of 1) Serial lesion area ($*10^4 \mu\text{m}^2$, n=9); 2) Lesion volume ($*10^7 \mu\text{m}^3$, n=9); 3) Mean lesion area ($*10^4 \mu\text{m}^2$, n=9). **G**, and **H**, Graphs show the measurements of 1) Lipid deposition (% of lesion area, n=9); 2) Collagen content (% of lesion area, n=9). **I**, and **J**, Graphs show the measurements of 1) Intraplaque hemorrhage (% of lesion area, n=9); 2) Necrotic core (% of lesion area, n=9). Each circle/triangle represents the average specific parameter of 8-11 sections in each mouse or the average lesion area of 9 mice at the indicated level in (**D**). Data are presented as mean \pm SEM and 'n' refers to the number of mice. n.s. is short for not significant, * $p < 0.05$ [two-sided Chi-square with Yates' correction for (B); two-tailed unpaired Student's *t* test for (E-J)].

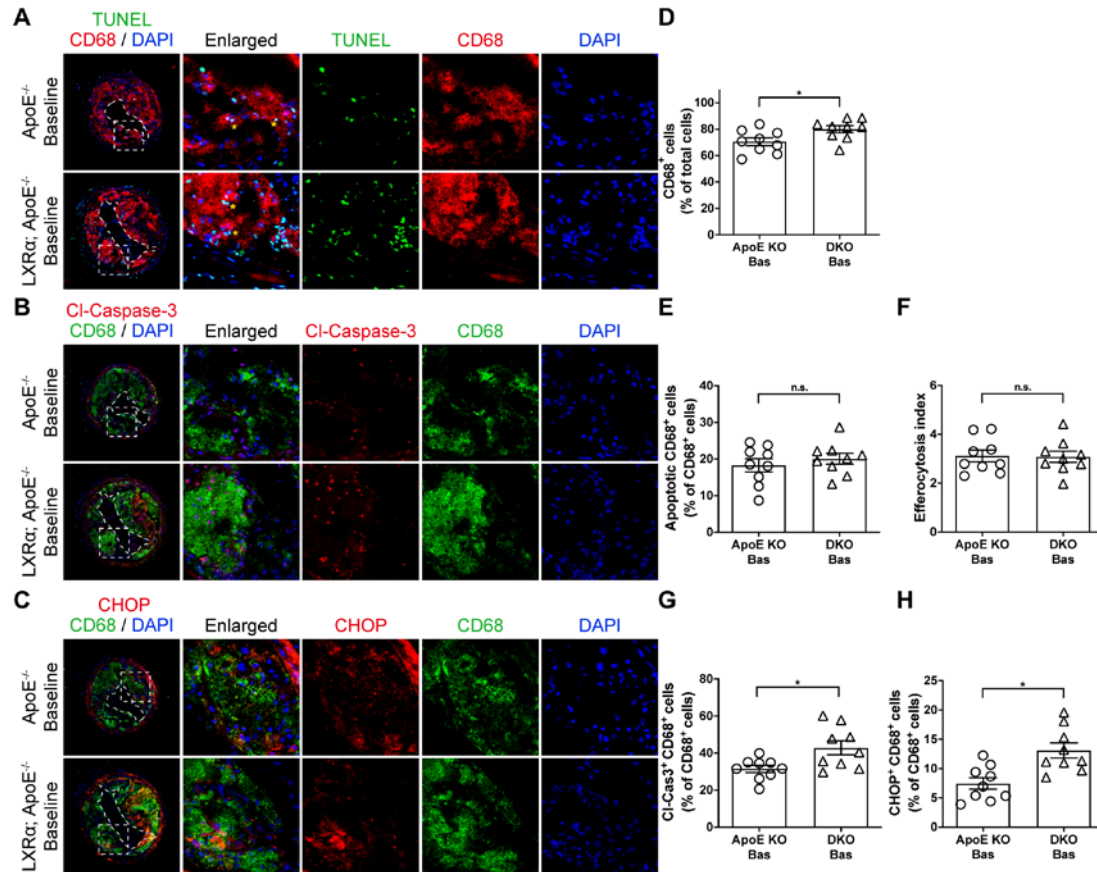


Figure S10. Biological features of lesional macrophages in ApoE^{-/-} and LXRα^{-/-} ApoE^{-/-} mice at 4 weeks.

Apoptosis, efferocytosis, and ER stress were evaluated. **A**, Representative immunofluorescence staining of macrophage apoptosis and efferocytosis in carotid sections is shown. Macrophages were stained with an anti-CD68 antibody (red), and apoptotic cells were stained with TUNEL (green). Yellow asterisks show examples of macrophage-associated apoptotic cells, while green asterisks indicate free apoptotic cells. Scale bar= 100 (first column) and 25 (second column) μ m. **B**, Representative photomicrographs of carotid sections stained with antibodies against CI-Caspase-3 (red) and CD68 (green), and counterstained with DAPI (blue). Scale bar= 100 (first column) and 25 (second column) μ m. **C**, Representative photomicrographs of carotid

sections stained with antibodies against CHOP (red) and CD68 (green), and counterstained with DAPI (blue). Dotted squares (first column in A, B, and C) indicate the corresponding part of the enlarged pictures (second column in A, B, and C). Scale bar= 100 (first column) and 25 (second column) μm . **D**, Graph shows the quantification of CD68⁺ cells (% of total cells, n=9). **E**, and **F**, Graphs show the quantification of apoptotic CD68⁺ cells (% of CD68⁺ cells, n=9) in (E) and the measurement of efferocytosis index (n=9) in (F). The efferocytosis index is the macrophage-associated apoptotic cells/free apoptotic cells. **G**, Graph shows the quantification of Cl-Cas3⁺CD68⁺ cells (% of CD68⁺ cells, n=9). **H**, Graph shows the quantification of CHOP⁺CD68⁺ cells (% of CD68⁺ cells, n=9). Dotted lines denote the lumen areas. Data are presented as mean \pm SEM and 'n' refers to the number of mice. n.s. is short for not significant, * $p < 0.05$ [two-tailed unpaired Student's *t* test for (D-H)].

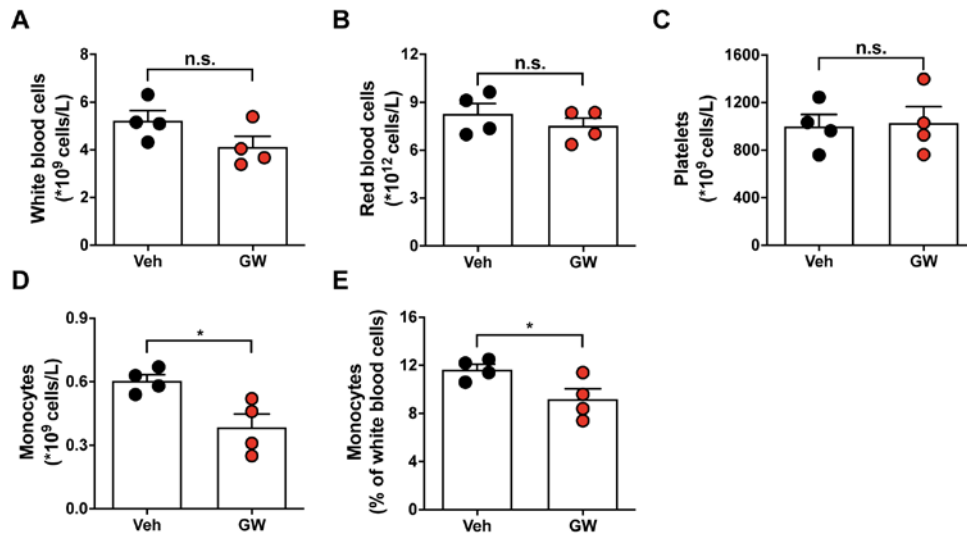


Figure S11. Quantification of complete blood counts.

Freshly obtained EDTA blood was used to measure complete blood counts (n=4). **A**, Graph shows the number of white blood cells (*10⁹ cells/L). **B**, Graph shows the number of red blood cells (*10¹² cells/L). **C**, Graph shows the number of platelets (*10⁹ cells/L). **D**, Graph shows the number of monocytes (*10⁹ cells/L). **E**, Graph shows the ratio of monocytes (% of white blood cells). Data are presented as mean ± SEM and 'n' refers to the number of mice. n.s. is short for not significant, *p < 0.05 [two-tailed unpaired Student's *t* test for (A-E)].

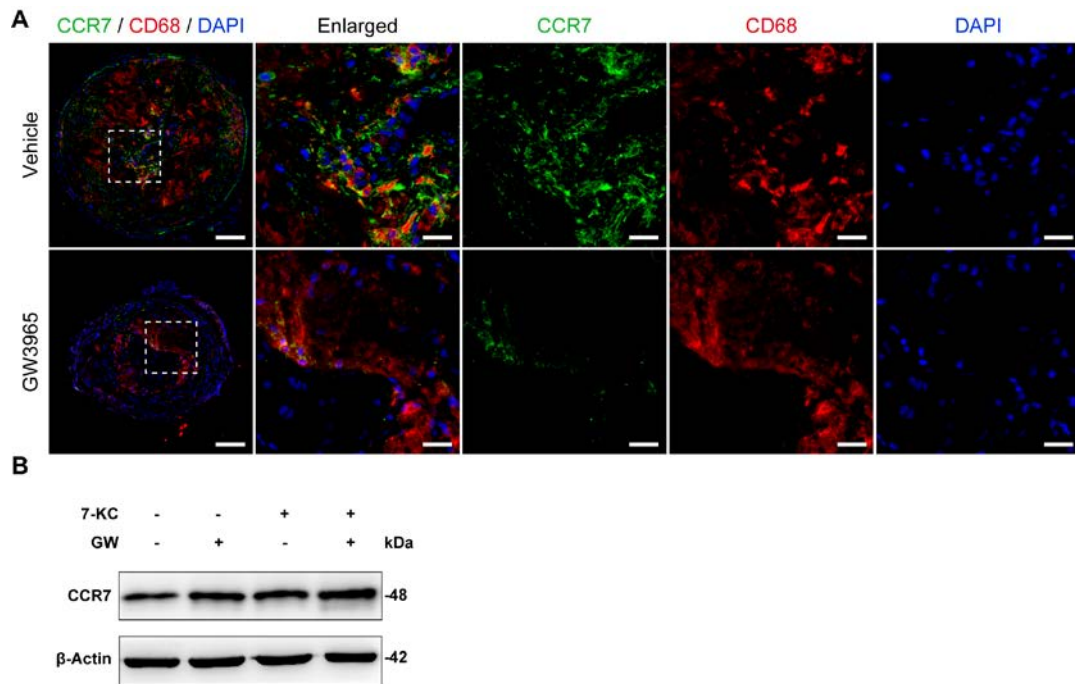


Figure S12. Measurements of plaque and macrophage CCR7 expression.

Immunofluorescence staining and western blotting assay were adopted to detect plaque and macrophage CCR7 expression, respectively. **A**, Representative photomicrographs of carotid sections stained with an antibody against CCR7 (green) and CD68 (red), and counterstained with DAPI (blue). Dotted squares (first column in A) indicate the corresponding part of the enlarged pictures (second column in A). Scale bar= 100 μ m. **B**, Western blotting of CCR7 protein expression in macrophages.

Supplemental References

46. Schrijvers DM, De Meyer GR, Kockx MM, Herman AG, Martinet W. Phagocytosis of apoptotic cells by macrophages is impaired in atherosclerosis. *Arterioscler Thromb Vasc Biol.* 2005;25:1256-1261
47. Kojima Y, Volkmer JP, McKenna K, Civelek M, Lusis AJ, Miller CL, Direnzo D, Nanda V, Ye J, Connolly AJ, et al. Cd47-blocking antibodies restore phagocytosis and prevent atherosclerosis. *Nature.* 2016;536:86-90
48. Seneviratne AN, Edsfeldt A, Cole JE, Kassiteridi C, Swart M, Park I, Green P, Khoyratty T, Saliba D, Goddard ME, et al. Interferon regulatory factor 5 controls necrotic core formation in atherosclerotic lesions by impairing efferocytosis. *Circulation.* 2017;136:1140-1154
49. Proto JD, Doran AC, Gusarova G, Yurdagul A, Jr., Sozen E, Subramanian M, Islam MN, Rymond CC, Du J, et al. Regulatory t cells promote macrophage efferocytosis during inflammation resolution. *Immunity.* 2018;49:666-677.e666